TUDelft

Delft University of Technology

Multi-Element Airfoil in Jet Flows

Identifying Dominant Factors and Interactions

Duivenvoorden, R.R.; Sinnige, T.; Veldhuis, L.L.M.; Friedrichs, Jens

Multi-Element Airfoil in Jet Flows: Identifying Dominant Factors and Interactions

Ramon R. Duivenvoorden,* Tomas Sinnige,† and Leo L. M. Veldhuis‡
Delft University of Technology, 2629 HS Delft, The Netherlands
and
Jens Friedrichs§
Technical University of Braunschweig, 38108 Braunschweig, Germany

Propeller–wing–flap systems are subject to complex aerodynamic interactions between each part of the system. Although the propeller–wing interaction in cruise conditions is well defined, the high-lift condition is relatively unexplored. Effective analysis of the complex aerodynamic relationship between propeller, wing, and flap is being impeded by a lack of understanding of the underlying mechanisms. In this paper, we therefore investigate the effects of a 2D jet impinging on a multisection airfoil. We quantify which factors that define a jet–wing–flap configuration dominate lift, drag, and moment responses. We further investigate interactions between these factors and discuss how they affect the flow. We find that the jet velocity ratio is by far the dominant factor in lift, drag, and moment responses, but it does not have strong interactions with other factors. The sensitivities of the multi-element airfoil do not change significantly when impinged upon by a jet, except when critical Mach numbers are exceeded. This strongly affects the aerodynamic response and dominant sensitivities. We furthermore conclude that the immersion of the flap is a key aspect when it comes to augmenting the lift by increasing the dynamic pressure in the flowfield. The conclusions from this paper can provide key insights for propeller–wing–flap flows.

I. Introduction

TO MEET the objectives of sustainable aviation, future aircraft designs will increasingly depend on leveraging the aerodynamic advantages of integrating propulsion with the airframe. This integration is crucial for enhancing aerodynamic efficiency, especially considering challenges such as limited battery energy density [1]. A promising approach involves utilizing (distributed) propellers as an active high-lift mechanism, capitalizing on the propeller–wing interaction (PWI) to augment lift. This strategy aligns well with the scalability of electric motors. By employing propellers to actively blow air over the wing, significantly greater lift coefficients can be achieved compared to traditional passive high-lift mechanisms [2]. Consequently, there's potential for reducing wing area requirements, typically determined by stall speed and maximum achievable lift [3]. This reduction in wing size can, in turn, enhance the aircraft's aerodynamic efficiency during cruise [4].

Until recently, the focus of PWI research has been on the cruise condition, for which the interactive effects between propellers and wings are now generally understood due to the contributions of, among others, Jameson [5], Kroo [6], Witkowski et al. [7], and Veldhuis [8]. Over the last decade, attention has shifted toward the high-lift regime. Many recent studies focus on variations of configurations with a tractor propeller and wing with a single slotted flap (e.g., [9–12]). The combination of propeller, wing, and flap benefits from both PWI and multi-element aerodynamics (the latter of which are described by Smith [13]). This enables lift coefficients that exceed those of even the most advanced passive high-lift configurations, which often feature three or more elements and are associated with significant mechanical complexity and weight. A popular example is the Maxwell X-57 aircraft developed by NASA [3], demonstrating the benefit of optimizing wing sizing for cruise.

Extensive research on propeller-blowing of high-lift wings already took place between 1950 and 1970, but aimed toward achieving fixed-wing vertical takeoff and landing (VTOL) capability. Notable contributions include the work of Kuhn and Draper (e.g., [2,14–16]) and the development of the Ryan XV-3RY, which remains the only fixed-wing VTOL aircraft to undergo flight testing [17]. However, much of this research focused on complex systems involving numerous slats, vanes, and flaps, with limited methods available for detailed study of flow structures. The emphasis was primarily on the turning ratio of the propeller slipstream, which affects the tilt of the resultant vector. Detailed descriptions of the aerodynamic phenomena occurring in the propeller–wing(–flap) interaction were lacking. In previous work [18], the authors demonstrated that complex aerodynamic phenomena occur during high-lift PWI that are either absent or less prominent during PWI in cruise conditions. The underlying mechanisms driving these complex flows are not yet fully understood.

A common trend in the current state-of-the-art of high-lift PWI is to approach the problem from a top-down perspective. Realizing the complexity of the complete system, it is assumed that analysis requires an integrated approach and cannot be approached as a sum of its parts. While this may be true, it also leads to difficulty in determining the origin of observed trends in the performance of the entire system. The field of high-lift PWI would therefore benefit from more fundamental analyses, identifying how different elements of the systems affect aerodynamic performance. The major component of complexity in active high-lift is the three-dimensional character of the propeller slipstream. However, from the early research on fixed-wing VTOL and their focus on the slipstream turning ratio, one can hypothesize that the primary variable in lift augmentation is the additional

*Ph.D. Candidate, Faculty of Aerospace Engineering, Department of Flow Physics and Technology; also Institute of Flight Propulsion and Turbomachinery, Technical University of Braunschweig, 38108 Braunschweig, Germany; also Cluster of Excellence "Sustainable and Energy-Efficient Aviation - SE²A" EXC 2163/1, Technical University of Braunschweig, Germany; r.r.duivenvoorden@tudelft.nl. Member AIAA.

†Assistant Professor, Faculty of Aerospace Engineering, Department of Flow Physics and Technology; also Cluster of Excellence "Sustainable and Energy-Efficient Aviation - SE²A" EXC 2163/1, Technical University of Braunschweig, Germany; t.sinnige@tudelft.nl. Member AIAA.

‡Full Professor, Faculty of Aerospace Engineering, Department of Flow Physics and Technology; j.friedrichs@ifas.tu-braunschweig.de. Member AIAA.

§Full Professor, Institute of Flight Propulsion and Turbomachinery; also Cluster of Excellence "Sustainable and Energy-Efficient Aviation - SE²A" EXC 2163/1, Technical University of Braunschweig, Germany; l.l.m.veldhuis@tudelft.nl. Member AIAA.

total pressure introduced by the propeller, while three-dimensional aspects such as swirl can be considered loss mechanisms. The most elementary representation of high-lift PWI would then be a two-dimensional multi-element airfoil subjected to an upstream jet flow.

This paper investigates the performance of a two-element airfoil in a jet flow and how this performance is affected by various design parameters. We find the main parameters that dominate the performance and pay special attention to important interactions between parameters. Furthermore, we investigate how the aerodynamic behavior of a multi-element airfoil changes when subjected to a jet compared to uniform flow. The results from this paper can serve as a basis for understanding the more complex interactions that occur in three-dimensional high-lift PWI flows.

II. Methods

We performed a parametric study with aerodynamic simulations of a two-element airfoil impinged upon by a uniform jet. This represents a simplified, two-dimensional equivalent of a propeller–wing–flap (or rather *jet–wing–flap*) configuration. The simulations presented in this paper are performed with a modified version of the 2D flow solver MSES, the details of which are discussed in Sec. II.A. A selection of configurations is also simulated using a RANS-based method, to test the validity of the MSES solver within the chosen parametric space and to verify the modifications made to the MSES code to include the jet. The RANS setup is described in Sec. II.B and the verification itself is found in Sec. III. We defined a parametric design space based on design of experiments (DoE) and analyzed it using response surface methodology (RSM) to identify relationships between the parameters and the performance characteristics. These are described in Secs. II.C and II.D, along with the choice of airfoil and the chosen parameters.

A.   Main Aerodynamic Solver

The primary solver used in this study is a modified version of MSES. It is a very computationally efficient solver, with average solution times in the order of minutes per configuration on a single CPU core. Since the streamline grid is part of the solution, it does not require predefined meshing for each configuration, making it very convenient for a parametric study. Another advantage of the streamline grid is that the location of the jet can be forced, which is expanded upon in Sec. II.A.1. The downsides are its numerical instability and its inherent assumptions. The first is improved by an automated solver process at the cost of some computational efficiency, discussed in Sec. II.A.3. The second is addressed by a verification using a set of RANS simulations, discussed in Sec. III.

1.   Solver Setup

MSES employs an inviscid, compressible streamline grid coupled to a viscous boundary-layer model based on the integral boundary-layer equations. For a description of the basic functionality of MSES, we refer to the original literature by Drela [19,20] and the User's Guide [21]. The global variables and constraints are set to default as suggested by the User's Guide [21]. For the conservation law, entropy is conserved for all cells except those where dissipation contributes significantly to the loss of total pressure. All simulations are run on a domain of 30 by 30 chords (meaning a boundary distance of 15 chords with respect to the airfoil leading edge), with 81 streamlines in the top and bottom domains, 51 streamlines between element stagnation lines, and 221 divisions per side on each airfoil. Due to the high lift coefficients that occur in the design space, the boundaries of the domain cannot be assumed as far field, as significant pressure gradients still remain on the domain exit and streamlines are not yet parallel to the freestream. Therefore, the vortex + source + doublet far-field boundary conditions are used (which are the default for MSES).

Using the resources for an actuator disk condition already present in the source code, we implemented a total pressure jump at a specified location on the domain inlet, thereby creating a parallel, uniform 2D jet. Although the jet is initiated at the inlet, its position is controlled by a *jet constraint* perpendicular to the reference chord line positioned one chord length in front of the leading edge. The solver finds streamtubes that cross the jet constraint and adds the total pressure to their inlet position, after which it marches the grid to the next iteration. This ensures that the airfoil is predictably immersed in the jet, despite the dependency of jet development on wing circulation. Figure 1 provides an illustration of the jet positioning.

To capture the edge of the jet and the associated velocity gradient accurately, a refinement of streamlines is required at the jet edge. This is implemented by including a refinement in the grid initialization step of the solver, where the total pressure jump is not yet specified. The addition of the total pressure contracts that portion of the grid as it increases the local dynamic pressure, which needs to be compensated for in the grid initialization as shown in Fig. 1a. Because this compensation—much like the jet development itself—is a function of the airfoil lift, the refinement may not end up exactly where expected, and the procedure is iterated until the center of the refinement is positioned within 5% of the jet size from the edge of the jet constraint. The density of streamlines around the refinement position then ensures that the solver resolves the jet edge accurately.
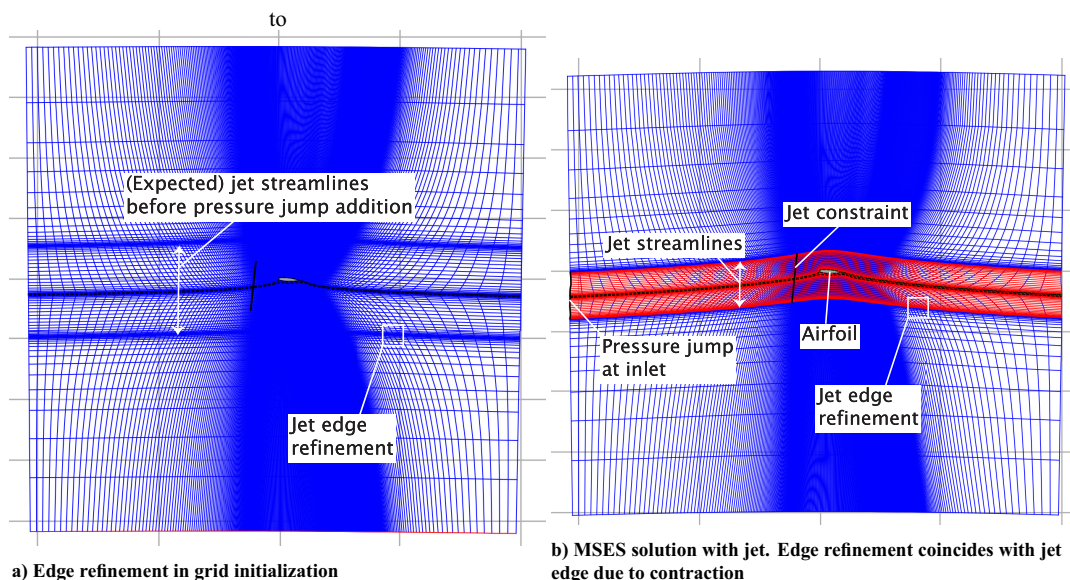

a) Edge refinement in grid initialization

b) MSES solution with jet. Edge refinement coincides with jet edge due to contraction

Fig. 1   Illustration of the jet constraint, total pressure addition, and edge refinement in the MSES grid.

2. Boundary-Layer Transition

MSES employs a hybrid viscous-inviscid formulation, where the viscous boundary layer is modeled by the integral boundary layer (IBL) equations. Furthermore, it uses an e^n-transition model to determine the state of the boundary layer, where n is a measure of the inherent turbulence of the flow. It also allows for the specification of fixed transition points in the boundary layer on each side of each element. For an airfoil in the slipstream of a propeller, it is commonly assumed that the boundary layer is fully turbulent. Unfortunately, many configurations in this study suffered from numerical instability when fixing the transition point. Instead, free transition was applied with a very low value of n. As a result, the suction-side boundary layer on the main element becomes turbulent within $0.05c$ for all configurations in the design space. The pressure side boundary layer and the flap boundary layers have a wider range of transition locations. When analyzed against the reported displacement thickness, however, the transition point does not have a dominant effect on the configurations in this study. We therefore assume that the boundary-layer state has a negligible impact on the reported aerodynamic coefficients, with the exception of friction drag due to the transitional nature of the boundary layer in MSES.

3. Solution Dependencies

The addition of the jet to MSES increases the inherent numerical instability of the solver, causing frequent nonconvergence, particularly when high streamline curvature or separation occurs. To mitigate this, the solver was set up to detect nonconvergence and automatically re-initiate the simulation with slight variations to the value of n for the transition method or the α at which the solution is initiated. The value of n is initiated at 2.0 and is allowed to vary up to 3.0 before complete nonconvergence is reported, while the initial α was reduced to a maximum of 3 deg. The relaxation of these parameters greatly improved convergence. Whereas the change in initial α does not affect the result, as it is always marched to the target value, in the case of n it has some impact on the solution.

For a given configuration, we found the lift and moment coefficients would vary up to 0.5% depending on the value of n_{crit}. Drag coefficient is, predictably, more affected and varies up to 2.5%. However, most of the deviation is found for $n_{\mathrm{crit}} > 2.5$ and all solutions remain within 0.5% deviation below that. Only 7% of the solutions in the datasets analyzed in this paper required $n_{\mathrm{crit}} > 2.5$ to converge and thus the effect of differences in n_{crit} on the analyses is limited.

An additional source of grid dependence is introduced by the addition of jet refinement. MSES initializes a predetermined number of streamlines in the grid in five different domains, split by the jet edge refinement location and airfoil stagnation lines, bound by the upper and lower limits of the domain. The distribution of streamlines within the jet is dependent on the alignment between the jet and the airfoil stagnation lines, which introduces some grid dependency into the results. We investigated the sensitivity of the solution to the number of streamlines, the number of airfoil divisions, and the jet refinement distribution algorithm and found that lift, drag, and moment coefficients remained within 1% of the reference solution.

B. RANS-Based Verification

We verified the implementation of the jet in MSES by comparing the results of RANS-based simulations. This also allows us to test the validity of some of the inherent assumptions made in MSES, which are not present in RANS-based solvers. Assumptions such as the lack of viscosity outside of the boundary layers and the lack of boundary-layer confluence on the flap may significantly affect the resulting wing lift, drag, and moment coefficient. The results of MSES and RANS for a selection of configurations are compared and discussed in Sec. III. A grid convergence study of the RANS simulations can be found in the Appendix.

1. Solver and Mesh Settings

We performed the RANS-based simulations with ANSYS Fluent 2020 R2, on an unstructured triangular mesh with Spalart–Allmaras

turbulence model. The fluid was compressible, and its viscosity was calculated according to Sutherland's law. The solver was set to pseudo-transient, with least squares-based gradient discretization and third-order schemes on all values except for turbulent viscosity, which was set to second-order upwind. The rectangular domain was 200 by 200 chords, angled to be aligned with the specified angle of attack. The upper and lower boundaries were specified as slip walls, while the inlet and outlet were configured as a total pressure inlet and an average static pressure outlet, respectively. The freestream was specified by the total pressure on the inlet, and the chord length was set to satisfy the Reynolds number at the specified freestream Mach number. The jet was implemented by a constant total pressure jump within the domain using the *fan boundary condition* (hereinafter referred to as *disk*) at the same location as the inlet location of the jet in MSES. In MSES, the grid contracts automatically around the pressure jump on the inlet, yielding a fully contracted jet throughout the domain. The RANS-based simulation requires a much larger grid, however, and thus the contraction of the jet occurs within the domain. The height of the disk was corrected for this contraction based on a simple conservation of mass calculation, such that the fully contracted jet has the same size as the MSES simulation.

The mesh was unstructured and triangular, with two areas of refinement, as shown in Fig. 2. The size of the *jet refinement box* was based on the streamlines extracted from the MSES results, scaled to twice the width of the disk (including compensation for contraction). It starts half the disk size ahead of the total pressure jump, continuing up to 10 chords downstream of the airfoil. The boundaries of the *wake refinement box* were straight lines at an angle of 5 deg from each other and tangential to the *jet refinement box*. The wake refinement was necessary to stabilize the continuity residuals. Both the main and flap elements feature inflation layers with a first layer height to satisfy $y^+ \approx 1$. The growth rate of the inflation layers was set to 1.15, and the number of layers was defined manually to achieve a smooth transition to the unstructured part of the mesh.

The mesh was discretized by maximum element size relative to the main airfoil element size. This ensured the mesh generation was similar for different chord lengths, which were varied between verification points (VPs) to satisfy the target Reynolds number. It also enabled a simple manner of consistent mesh refinement for grid convergence studies (detailed in the Appendix). In the finest grid, which is used for all comparisons with MSES in this paper, the main airfoil element was divided into 1493 elements. Table 1 summarizes the relationships between the element sizes specified in the grid generation. The maximum element size of the outer domain is left at the solver default (which depends on the freestream condition), and the global mesh growth rate is 1.05.

C. Definition of the Experimental Setup

The jet–wing–flap setup considered in this study is illustrated in Fig. 3. It consists of nine design parameters, hereinafter referred to as *factors*. These factors include: the flap gap (ds), overlap (dx) and deflection angle (δ_f), as well as the intersection position of the jet with respect to the main airfoil (z/D). The jet is initiated far upstream of the airfoil, depending on a specified intersection location within the domain. This location is perpendicular to the airfoil chord line and positioned at one chord length from the leading edge. The factors that complete the parametric space are the angle of attack (α), freestream Reynolds (Re) and Mach (M) number, and the velocity in the jet normalized by the freestream velocity (V_j/V_∞).

We consider the NLR 7301 airfoil with a separate downstream flap. This airfoil was taken from van den Berg and Oskam [22] and is a transonic design with a relatively large leading-edge radius and no flap-nested position. It thus avoids a cove and associated separation, which is beneficial to the convergence of MSES.

1. Central Composite Design

The test matrix considered in this study is defined by a k-factor central composite design (CCD). It consists of a 2^k factorial design with $2\dot{k}$ star points to test for curvature and one centerpoint. For the nine-factor design of this study, this results in a total of 531 configu-
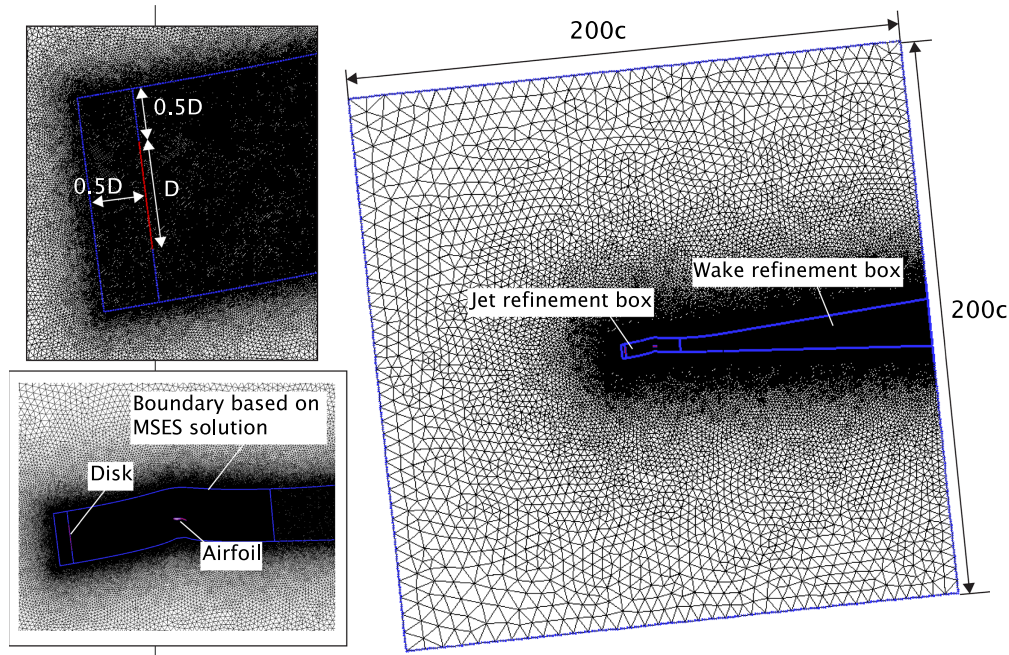
Fig. 2   Illustration of RANS mesh setup showing the refinement areas.

Table 1   Mesh discretization settings

Element sizing	Relation
Main element (d_{main})	$c/1493$
Flap element	$d_{main}/1.5$
Trailing edges	$d_{main}/12$
Jet refinement	$d_{main} * 5$
Wake refinement	$d_{main} * 10$

rations. As the data are obtained from deterministic simulations, only a single centerpoint is necessary. Further information on CCDs can be found in classic textbooks on DoE, such as Montgomery [23], and will not be expanded upon in this paper. The resulting CCD is summarized in Table 2 and motivated in Sec. II.C.2. The upper and lower bounds of each factor in the factorial part of the CCD (also called the *high* and *low* settings), along with their star points, are summarized in Table 2 and motivated in Sec. II.C.2. In the remainder of this paper, we will refer to this full nine-factor design space as the *jet design*.

The main objective of this paper is to identify and quantify the dominant factors and interactions of the jet–wing–flap system, which requires an orthogonal design to be able to fully separate the contributions of each factor and interaction. The orthogonality of the design is achieved by the specific placement of the star points. Unfortunately, the star points required for a fully orthogonal nine-factor design are beyond the physical limitations of the configurations and the solver, unless the parametric space is severely constricted. We therefore restricted α^* to ± 1.7321, where α^* is the distance of the axial points to the centerpoint.¶ The multicollinearity that is introduced into the design in this way is minimal and will be treated in Sec. II.D.1.

The same CCD, but excluding the jet-related factors D/c, z/D, and V_j/V_∞, serves as a baseline for multi-element airfoil behavior in uniform flow. This *baseline design* thus considers six factors with 12 axial points and a centerpoint, resulting in a total of 77 configurations. Apart from the exclusion of the jet factors, factor ranges are equal

to those in Table 2. The baseline design is compared with *subset designs*, which follow the same CCD as the baseline design but include a jet of fixed V_j/V_∞, D/c, and z/D in their domain. These thus represent a small portion of the full jet design and allow for direct comparison with the baseline (performed in Sec. IV.A.1).

2.   Choice of Factor Ranges

The factor ranges for the CCD were chosen to represent a full-scale transport aircraft with highly loaded propellers in takeoff configuration. Subsequently, the factor ranges were restricted based on solver limitations and to maintain design orthogonality. Design orthogonality is further discussed in Sec. II.D.1. The solver limitations restricted the use of high angles of attack, as the solver would not reliably converge when approaching $C_{l,\max}$. Furthermore, the Mach number is chosen to avoid shocks in the majority of the design, as they also affect solver reliability negatively.

The factor range of the flap deflection, gap, and overlap was centered close to the original design of the flap of 20° with 5.3% overlap and 2.6% gap, with some adjustments to the respective ranges to avoid unfeasible configurations within the design space (for instance, $d_x < d_s$ cannot be achieved for most flap deflections). Generally, we have aimed to maintain as wide a range as possible.

The vertical position of the jet relative to the airfoil is chosen such that the airfoil stagnation lines remain within the jet in any configuration in the design space. This is a limitation of the numerical setup and is explained further in Sec. II.A. Since the pressure jump is placed at the domain inlet, there is no contraction in the domain, and there is no streamwise dependency of the jet constraint.

The range of jet velocity ratios is based on the ratios considered in the work by Ting et al. [24], which are also used by Patterson et al. [25] in their work on lift-augmenting (distributed) propeller design. In the test matrix, the jet velocity ratios chosen are equivalent to thrust coefficients between $T_c \approx 0.29$ and ≈ 1.5, depending on other factors in the system, where $T_c = (T/\rho_\infty V_\infty^2 D_{prop}^2)$. This yields an overall relatively high T_c, with some configurations on the edges of the design space even becoming practically unfeasible. In the context of (distributed) propeller-blown high-lift augmentation, it is worthwhile to include relatively high thrust coefficients within the design space. Furthermore, high jet velocity ratios will make changes to the parametric sensitivities of the airfoil more pronounced. Configurations on the edge of the design space, even if practically unfeasible, test the potential nonlinearity of the theoretical responses.

¶In factorial designs, the centerpoint is zero, and the *high* and *low* settings of factors are defined as distance $+1$ and -1 from the centerpoint, respectively. The axial points are then at a distance of 1.7321 from the centerpoint.
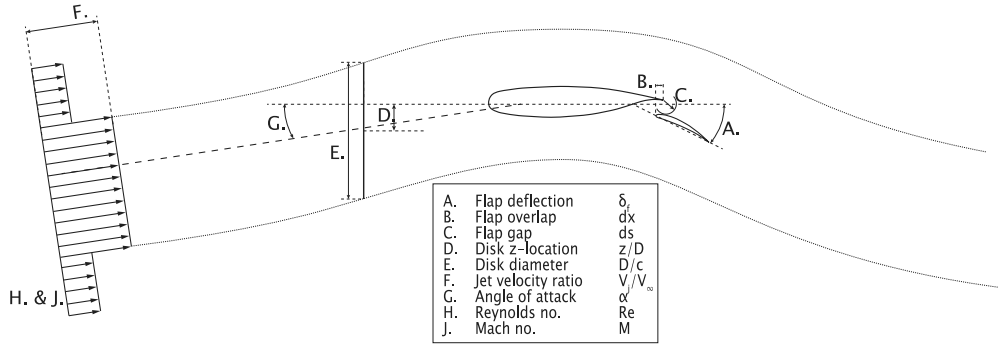
Fig. 3   Illustration of the parametric design space of the jet–wing–flap configuration.

Table 2   Overview of the setpoints of the full nine-factor central composite design

Coding	Factor	Unit	$-\alpha^{**}$ (−1.7321)	Low (−1)	Center	High (+1)	$+\alpha^*$ (+1.7321)
A	δ_f	deg	11.34	15	20	25	28.66
B	δ_x	deg	−0.02928	0	0.04	0.08	0.10928
C	δ_s	deg	0.022679	0.03	0.04	0.05	0.057321
D	z/D	— —	−0.30981	−0.2	−0.05	0.1	0.20981
E	D/c	— —	0.77058	1.1	1.55	2	2.3294
F	V_j/V_∞	— —	1.317	1.5	1.75	2	2.183
G	α	deg	0.5359	2	4	6	7.4641
H	Re	— —	5.44E+06	8.00E+06	1.15E+07	1.50E+07	1.76E+07
J	M	— —	0.1317	0.15	0.175	0.2	0.2183

D.   Identifying Dominant Factors and Interactions

We employ DoE and RSM principles to identify the dominant factors and interactions that govern the aerodynamic performance of the configurations in the design space. In this paper, we analyze the total lift, drag, and moment coefficients of the airfoil, as well as the lift coefficient of the main and flap elements separately and the lift augmentation factor K_{C_l}. The latter is defined as the ratio of lift coefficient with a jet in the domain compared to the same airfoil configuration without the jet. These performance coefficients are hereinafter referred to as *responses*.

Responses are always nondimensionalized based on the free-stream conditions, not the jet velocity. Note that these are responses relating to integral performance, not specific aerodynamic phenomena. Those have to be identified by aerodynamic analyses, for which the relationship between factors and performance coefficients can serve as effective guidance. We can also compare different design spaces, such as jet flow conditions with regular uniform freestream conditions, and test whether the dominant relations change. This would indicate fundamental changes in aerodynamic interactions.

1.   Definition of Metamodel

Fitting a regression model (or *metamodel*) to a set of datapoints maps a response (e.g., lift coefficient) to the factors and interactions considered in the metamodel. For the jet design, we use a standard quadratic metamodel extended with three-factor interactions, given by Eq. (1). We include three-factor interactions because the jet design contains factors related to two systems known to each include two-way aerodynamic interactions (propeller–wing and wing–flap). Significant three-factor interactions are therefore likely to occur. Each term in Eq. (1) (also referred to as *model term*) relates to a factor or an interaction between factors. For instance, the model term $\beta_{1,2}x_1x_2$ relates to the effect of the interaction of factors x_1 and x_2 on the response y, with $\beta_{1,2}$ being the gain obtained from the regression fit.

$$y = \beta + \sum_{i=1}^{p} \beta_i x_i + \sum_{i=1}^{p} \beta_{ii} x_i^2 + \sum_{i=1}^{p-1} \sum_{j=i+1}^{p} \beta_{ij} x_i x_j$$

$$+ \sum_{i=1}^{p-2} \sum_{j=i+1}^{p-1} \sum_{k=j+1}^{p} \beta_{ijk} x_i x_j x_k + \varepsilon \qquad (1)$$

We can rank the importance of each model term based on their relative contribution to the variance in response of all terms in the metamodel combined (or *total metamodel*). This is done by taking a ratio of the partial sum of squares of each term to the sum of squares of the total metamodel. This quantifies how much each term contributes to the total variability of the response across the design space. For a full overview of DoE/RSM, readers are again referred to standard textbooks on the topic, such as Montgomery [23]. Since the data considered in this study were obtained using deterministic numerical simulations, there is no random error. The typical approach using analysis of variance (ANOVA) to reduce the number of model terms cannot therefore be applied, and all terms are kept in the metamodel for the jet design.

For the baseline and subset designs, however, we excluded the three factor interaction terms of Eq. (1), leaving only the quadratic metamodel. Since the baseline and subset designs do not include jet parameters as factors, three-factor interactions are unlikely to be significant. We confirmed this by analyzing the baseline and some of the subset designs, both with the quadratic metamodel only and with the extended metamodel. In both cases, the dominant factors and interactions are identified with equal levels of contribution to the model. Three-factor interactions never contributed more than 0.14% to the baseline and subset models (with most three-factor interactions below 0.01%), unlike for the models for the full jet design (see Sec. IV.B.1).

2.   Multicollinearity

The main reason to exclude three-factor interactions from the metamodels for the baseline and subset designs was to reduce the multicollinearity of model terms in one of the subsets (with $V_j/V_\infty = 2.0$, see Sec. IV.A.1). For this design, not enough design points could be converged to include the three-factor interactions. Low multicollinearity is required to independently determine the contribution of each term in the metamodel [23,26]. The main purpose of the analysis in this paper is to determine the relative contribution of each model term to the chosen responses, rather than provide an estimation of the response for an arbitrary location within the parametric space. Therefore, we focus on minimal multicollinearity instead of optimal fit.

Multicollinearity of model terms can be measured by the variance inflation factor (VIF), where a VIF of one means the term is completely independent. Standard practice is to reject a model when the VIF of any term is greater than 10, or in more conservative cases, greater than 5 [26–28]. For all metamodels analyzed in this paper, the VIF remains below 3 for all model terms, ensuring the terms can be interpreted as independent.

3. Data Transformation and Model Fit

To improve the fit of the metamodel, we apply data transformations in the analysis according to the Box–Cox approach. This determines a power transformation of the response $y^\lambda + k$ (where y is the response data and λ and k are the power transform parameters) for which the error sum of squares is the minimum [23]. Response values reported in this document are always in the actual (nontransformed) space.

By applying the metamodel described by Eq. (1), we inherently assume that the factor dominance of the design space can be estimated using an extended quadratic model. Since all of the main factors individually have either a linear or quadratic relation to the chosen responses within the considered values, combined with the focus on term ranking instead of response prediction, we believe this assumption to be valid. As there is no random error in the design and replicates are meaningless in the context of deterministic simulations, we cannot perform a standard lack-of-fit test. We therefore verify the metamodel fit using 300 confirmation points distributed throughout the parametric space. The points are chosen according to the I-optimality criterion, which attempts to reduce the prediction variance in the design space and is thus expected to be most critical for model fit.

Figure 4 shows histograms based on the number of runs with a residual of the predicted value within a certain range of the simulated value. The cumulative fraction of the total number of runs is displayed on the secondary axis. The model for lift predicts over 95% of the model points with a residual of less than 1.5% and all of the model points within 3.5%. The models for drag and moment show more deviation, but they still predict 95% of the points within 5% of their actual value. All models show larger deviations for the confirmation points, although this is to be expected. Out of the confirmation points, 95% are predicted within 3.5% of their actual lift value, while their moment value is predicted within 4.5%. For drag, the 95% mark is reached with a maximum residual of around 7.5%. Toward the edge of the design space, particularly for the combination of high α, M, and V_j/V_∞, the prediction of drag becomes very poor. This is an indication of insufficient model order for that part of the design space. Nonetheless, based on the data in Fig. 4, we are confident the metamodels sufficiently represent the parametric space for the analysis in this paper. Only the drag response may become invalidated for configurations with high α, M, and V_j/V_∞. This is likely related to compressibility effects, which are further discussed in Sec. IV.

4. Note on Higher-Order Designs

The fit of the drag coefficient in Fig. 4 can certainly be improved and would likely benefit from a higher-order DoE. Although third-order CCDs exist (e.g., [29]), the distance requirements for the star points to achieve a fully orthogonal design are not feasible for the nine-factor parametric space considered in this study. Reducing the distance of axial points to feasible levels raised the VIF values of the main terms beyond 10, which is unsuitable for the intended analyses. We also evaluated the designs by Zhang et al. [30] and Yankam and Oladugba [31], who both propose augmentations to traditional CCD using orthogonal arrays to be able to fit third-order models but obtain similarly high VIF values. The same occurs for the nested face-centered design proposed by Landman et al. [32], who achieve a maximum VIF of 9. Although these designs allow for models with a closer fit to the response data due to their higher order, the lack of term independence would invalidate the analysis we perform in this paper. Unlike the experiments that the DoE/RSM principles were originally designed for, model reduction by removing statistically insignificant terms is not possible for deterministic numerical simulations due to the lack of random error. Designs focused on the type of multifactor higher-order analyses that are applicable to numerical studies would therefore be very much of interest for future research.

III. Verification of MSES for Jet–Wing–Flap Flows

Despite using resources available in the original source code, the inclusion of the jet required modifications not normally present in MSES. Therefore, a verification of the jet implementation is necessary. Furthermore, as MSES is not commonly used for jet flows, the inherent assumptions of the method require validation. Unfortunately, the setup cannot be reproduced experimentally. We therefore compare the results from MSES with RANS simulations for several configurations in the design space. Unlike MSES, RANS resolves much of the boundary layer, includes viscosity in the entire domain, and inherently captures boundary-layer confluence.

A. Verification Points

We selected five VPs based on configurations predicted by MSES to have maximum C_l, maximum and minimum C_d, and maximum and minimum L/D. These configurations represent extreme cases in aerodynamic performance according to MSES and are therefore likely to challenge the assumptions of the model. Large discrepancies between the MSES and RANS solutions would indicate violations of these assumptions. Additionally, these VPs encompass combinations of main factors that fill the design space well. Table 3 summarizes the design parameters of the VPs that we included in the verification.

B. Comparison Between MSES and RANS

Figure 5a shows the percentual difference between the RANS and MSES results: $\Delta_{(MSES-RANS)} = (MSES/RANS) - 1$. It compares lift, drag, and pitching moment coefficients for the total airfoil as well as for each element separately. From Fig. 5a, it is clear that both lift and moment coefficients match well between RANS and MSES, but drag coefficients match poorly. This may partly be explained by the transitional nature of MSES. Figure 5c shows that the friction drag
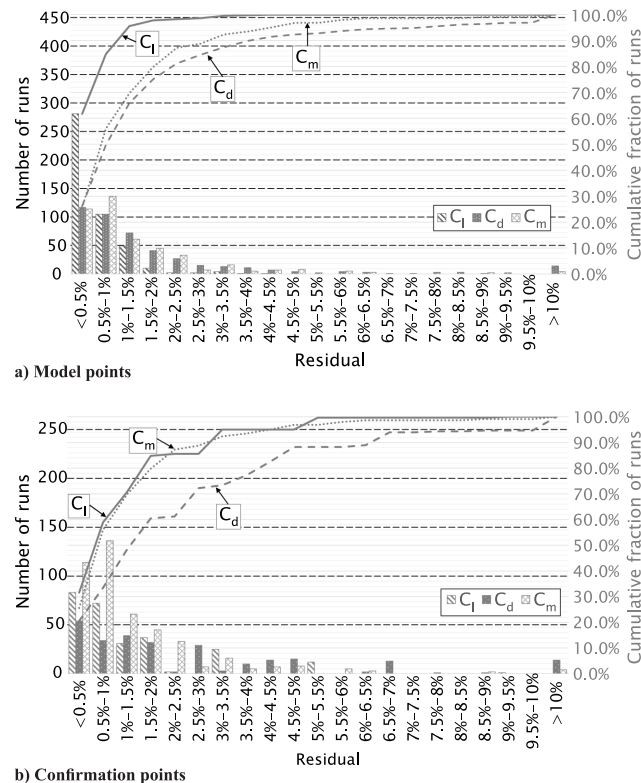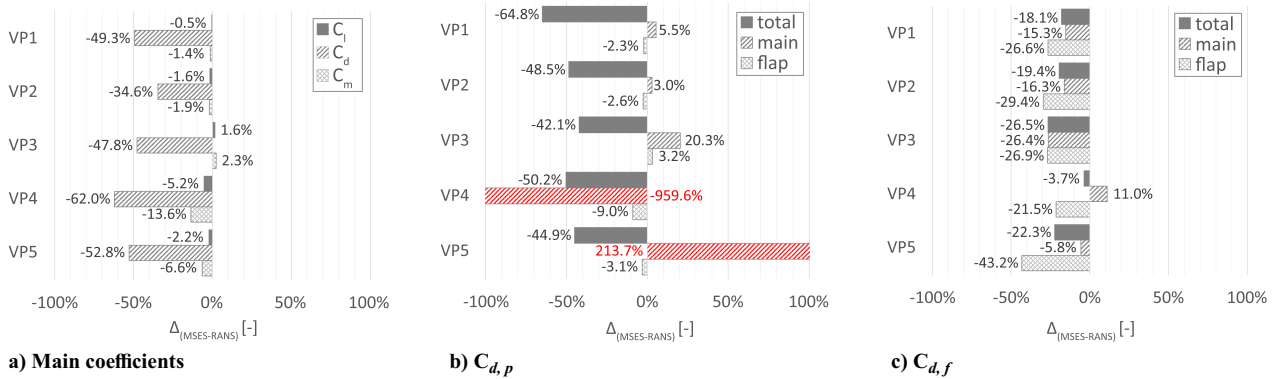

a) Model points

b) Confirmation points

Fig. 4 Histogram of the percentual residual of the model points and the confirmation points for the metamodels used in the regression analysis of the main design.

Table 3   Verification points chosen from the design space

VP	Description	δ_f, deg	δ_x	δ_s	z/D	D/c	V_j/V_∞	α, deg	Re	M	C_l^*	C_d^*	C_m^*
1	Max L/D	25	0.00	0.03	−0.2	2	2	2	$1.50e7$	0.15	8.634	0.0468	−2.329
2	Min C_d	20	0.04	0.04	−0.05	1.55	1.75	4	$1.15e7$	0.175	6.573	0.0417	−1.480
3	Max C_l	25	0.00	0.05	0.1	2	2	6	$8.00e6$	0.15	10.74	0.1107	−2.323
4	Max C_d	15	0.08	0.05	0.1	2	2	6	$1.50e7$	0.2	7.278	0.1372	−1.279
5	Min L/D	15	0.08	0.05	−0.2	1.1	2	6	$8.00e6$	0.2	6.794	0.1312	−1.232

* From MSES simulations.

Fig. 5   Deltas in coefficients predicted by MSES versus RANS. Comparison of main coefficients (a) and drag coefficients per element (b and c).

is systematically underestimated by MSES compared to RANS. Furthermore, the drag coefficient of multi-element airfoils is a combination of the large pressure drag contribution of each element. These contributions have opposite signs and add to a small resulting value. This means that small differences in the drag of each element can sum to large differences in the total drag coefficient, as illustrated by Fig. 5b. Although the pressure drag of each element matches well for most configurations, the percentual deviation of the total pressure drag is much larger.

VP4 and VP5 show a very large deviation of the main element pressure drag between the two methods. This can be traced to shock-induced separation bubbles occurring in the RANS simulations, as shown for VP4 and VP5 in Fig. 6. Although MSES predicts a significant jump in displacement thickness due to the shock, it does not show evidence of a separation bubble. This is best observed from the pressure distributions.
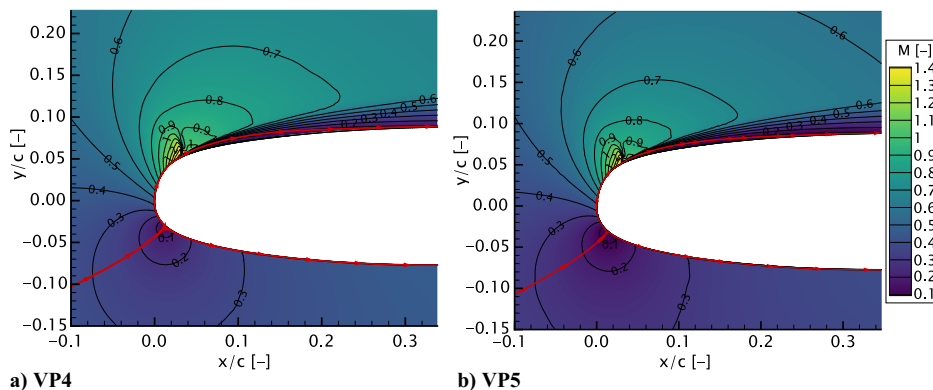
1.   Pressure Distributions

Figure 7 shows the pressure distributions from both MSES and RANS for each VP. VPs 1–3 show an excellent match between both methods, as should be expected from the close match in lift, pitching moment, and pressure drag coefficients. For VP4 and VP5, the RANS pressure distributions show the effects of the separation bubble as a thinner pressure peak with a change in its slope around $x/c = 0.03c$.

MSES shows no evidence of this, resulting in a stronger pressure peak and thus a much larger negative pressure drag component for the main element. This explains the deviation of pressure drag on the main element for VP4 and VP5. It should be noted that VP3 also has a transonic region at roughly the same location, but both MSES and RANS predict fully attached boundary layers, and the aerodynamic coefficients show excellent agreement between both methods. MSES is thus able to resolve the transonic region in certain conditions, but not when it induces local separation.

2.   Jet Velocity at the Constraint Location

The final metric we compare is the jet trajectory and velocity distribution, specifically the target position at $x/c = -1$. Since the pressure jump location in RANS is not iterated and the jet position at $x/c = -1$ is a function of airfoil circulation, it can be considered a metric of flowfield similarity between RANS and MSES.

Figure 8 shows the jet velocity profile at $x/c = -1$ for both methods. The gradient at the edge of the jet in the RANS solution, rather than a discrete jump as in the MSES solution, reveals the presence of viscous shear layers. From the gradients, we can see that the shear layers remain relatively thin close to the airfoil and do not influence the shape of the velocity distribution significantly. Overall, RANS and MSES predictions of the jet profile match very well.

a) VP4   **b) VP5**

Fig. 6   Mach contours around the main element leading edge and streamline showing separation bubble. RANS simulation.
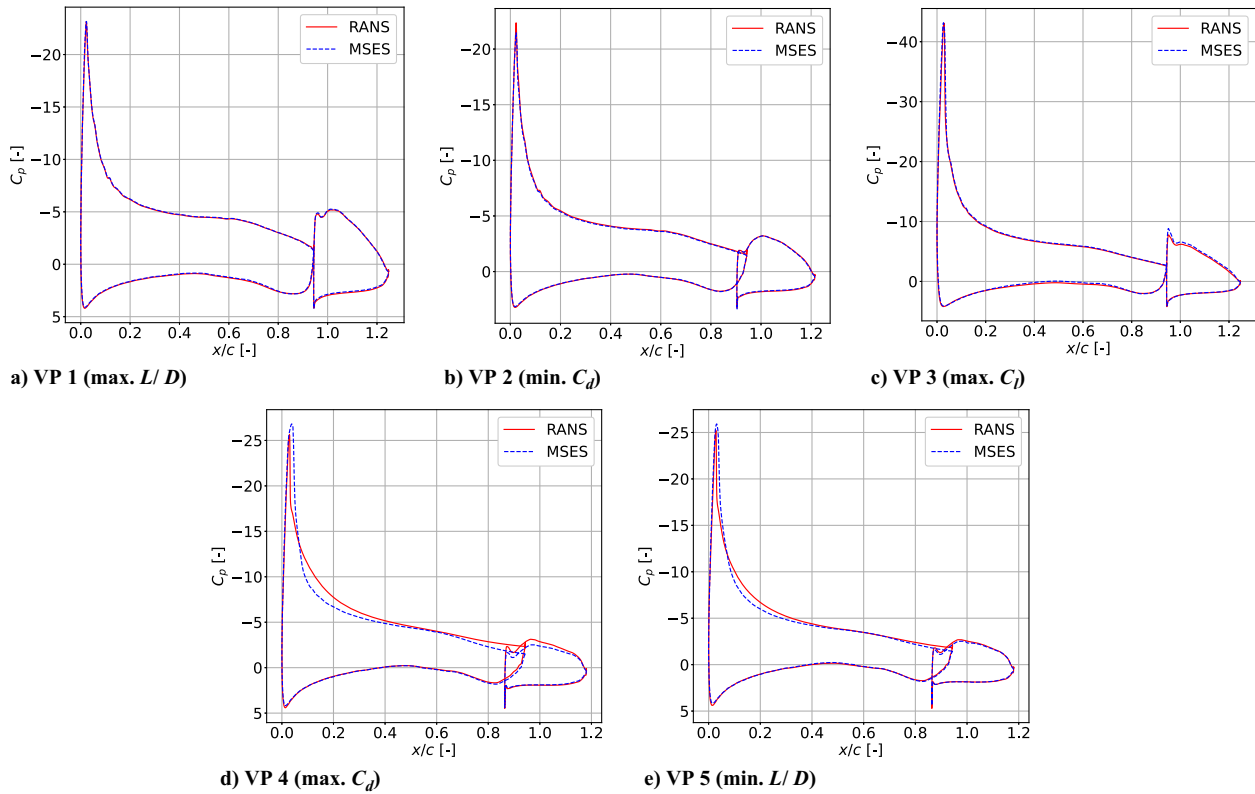
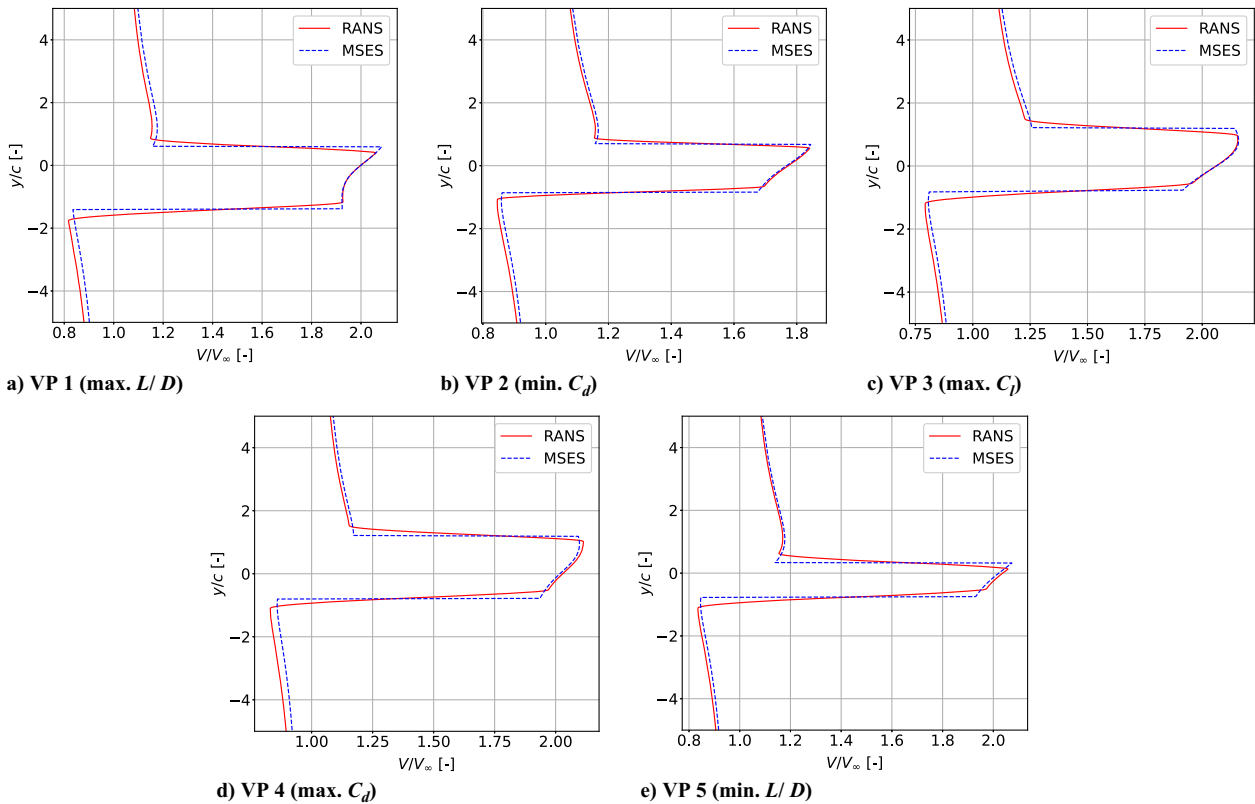**Fig. 7   Comparison of pressure distribution as predicted by MSES versus RANS.**

a) VP 1 (max. *L/ D*) b) VP 2 (min. *C_d*) c) VP 3 (max. *C_l*)

d) VP 4 (max. *C_d*) e) VP 5 (min. *L/ D*)

Fig. 8   Comparison of velocity at the jet constraint as predicted by MSES and RANS.

a) VP 1 (max. *L/ D*) b) VP 2 (min. *C_d*) c) VP 3 (max. *C_l*)

d) VP 4 (max. *C_d*) e) VP 5 (min. *L/ D*)

3.   *Reflection on Accuracy of Flow Modeling*

The presented metrics show that across the design space, configurations that are significantly different from an aerodynamic perspective are represented by MSES at a similar fidelity as provided by RANS. The assumption of inviscid flow outside of the boundary layer made by MSES does not appear to significantly change the solution in the verified cases. MSES consistently underestimates friction drag, likely a result of the transition model. Furthermore, it is not able to resolve shock-induced separation bubbles in the same manner as RANS. However, this does not dominate the drag

coefficient or the deviation between MSES and RANS. We therefore expect that the trends of drag coefficient in the design space are still captured with sufficient accuracy for the analysis in this paper, but note that the conclusions from this paper may require reassessment in the presence of stronger shocks.

IV. Results and Discussion

We simulated each configuration in the test matrix for the jet design and the baseline design and subsequently fitted metamodels to each of the responses in the corresponding design space. Based on the resulting metamodel equations, we calculated the contribution of each term in the equation to the model. This gives the contribution of each factor and interaction in the model to the variability of the modeled response across the design space. In this section, we present rankings of factors and interactions for each response based on their contribution to the model, as well as how the factors affect the responses. Finally, we reflect on the important interactions from an aerodynamic perspective and how the findings in this study affect design considerations for propeller–wing–flap systems.

A. Baseline Design Space Results

Figure 9 displays dominant term contributions in metamodels for lift, drag, and moment coefficients in the baseline design space without jet flow. The model term contribution quantifies how much of the variability of the response across the metamodel can be attributed to that term (see Sec. II.D). Only factors and interactions contributing at least 1% to any response are shown for clarity, with all terms retained in the metamodel. Model terms are represented by coded letters. For example, AD denotes the interaction between factors A (δ_f) and D (α) and its contribution is independent of the contribution of each factor individually. "Main factors" denote the sum of main factor contributions, excluding interactions. The main factors alone capture over 97% of the variability in each response, suggesting minimal interaction effects.

The factor contributions alone do not show how the factor affects the response in absolute terms. This is better visualized by a perturbation plot, as shown in Fig. 10, for the lift response. This plot depicts response deviations from a reference point (the centerpoint of the design space) as factors change individually. Lines show response changes when a single factor is varied between low (-1) and high ($+1$) values, while others remain constant. This does not show interactions, which would cause the trends to change depending on the value of interacting factors. Since Fig. 9 indicates no significant interactions, this suggests stable trends in the perturbation plot across the design space.

1. Comparison Between Uniform and Jet Flows

We can compare the baseline design with subsets of the jet design, where the jet-related factors V_j/V_∞, D/c, and z/D are kept constant. These subsets then have the same six-factor CCD as the baseline design. This will show us whether the airfoil responds differently to any of the factors and interactions when immersed in a jet compared
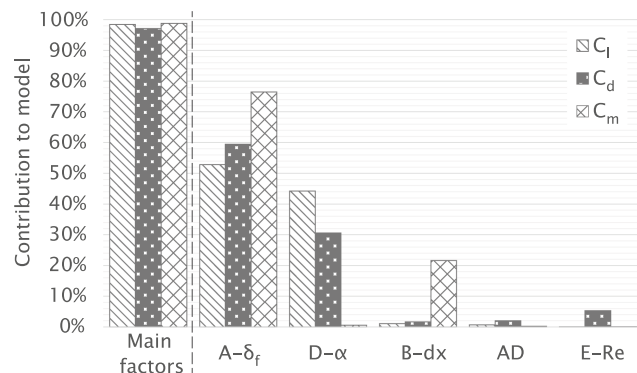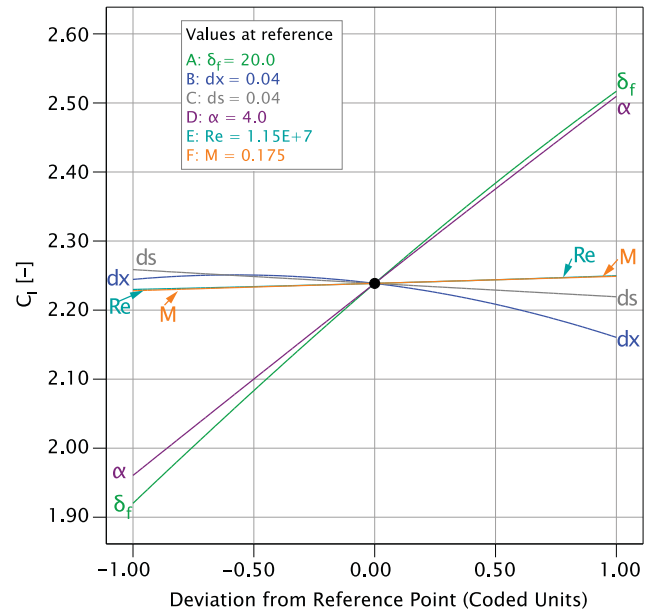
Fig. 10 Perturbation plot of lift coefficient around the centerpoint of the baseline model, showing how the response changes when each factor is varied independently between their low (-1) and high (+1) setting.

to uniform freestream. Figure 11 shows the factor contributions to the lift, drag, and moment responses for the baseline design space and subsets with various combinations of jet size, velocity, and position. Table 4 summarizes the four subsets considered in this paper, which represent different combinations of jet size, position, and velocity.

Figure 11 reveals that for low jet velocity ratios (subsets 1–3), the same factors and interactions contribute to the response as for the baseline, matching within a few percent of contribution. The slight differences between cases can be attributed to a combination of the inherent error of the solver and any interactions between the displayed factors and the jet position and velocity. For high jet velocity (subset 4), however, the factor contributions change significantly. Lift and moment coefficient responses show significant variations in the contribution of their dominant factors, but overall they show the same terms to be dominant. The Mach number and the interaction DF ($\alpha - M$) are added as significant contributors. For the drag response, however, the dominant terms change drastically. Flap deflection contributes much less to the model compared to the other subsets and the baseline, while Mach number becomes the second-most dominant factor. Interactions DF ($\alpha - M$) and AF ($\delta_f - M$) also significantly increase their contributions.

The change in the dominant factors and interactions for subset 4 can be attributed to the occurrence of transonic flow on the main element. This adds wave drag and can increase the boundary-layer displacement thickness (and thus viscous drag) significantly, as illustrated in Fig. 12. Out of all design points in subset 4, roughly 70% have a shock on the main element, with wave drag on average contributing 10% of the total drag. For the other subsets, only about 20% of the design points contain transonic flow, and the wave drag contributes, on average, only around 1% to the total drag. The baseline design contains no configurations with transonic flow at all. The occurrence of transonic flow is, of course, highly configuration dependent, and the jet velocity ratios considered in this study are relatively high. Nonetheless, the addition of a jet to the domain can trigger a significantly different airfoil response compared to a uniform flow due to transonic effects. This may pose a crucial limit to propeller blowing as a high-lift system.

B. Jet Design Space Results

Figure 13 shows the relative contributions of model terms to the responses in lift, drag, and moment coefficients for the full jet design
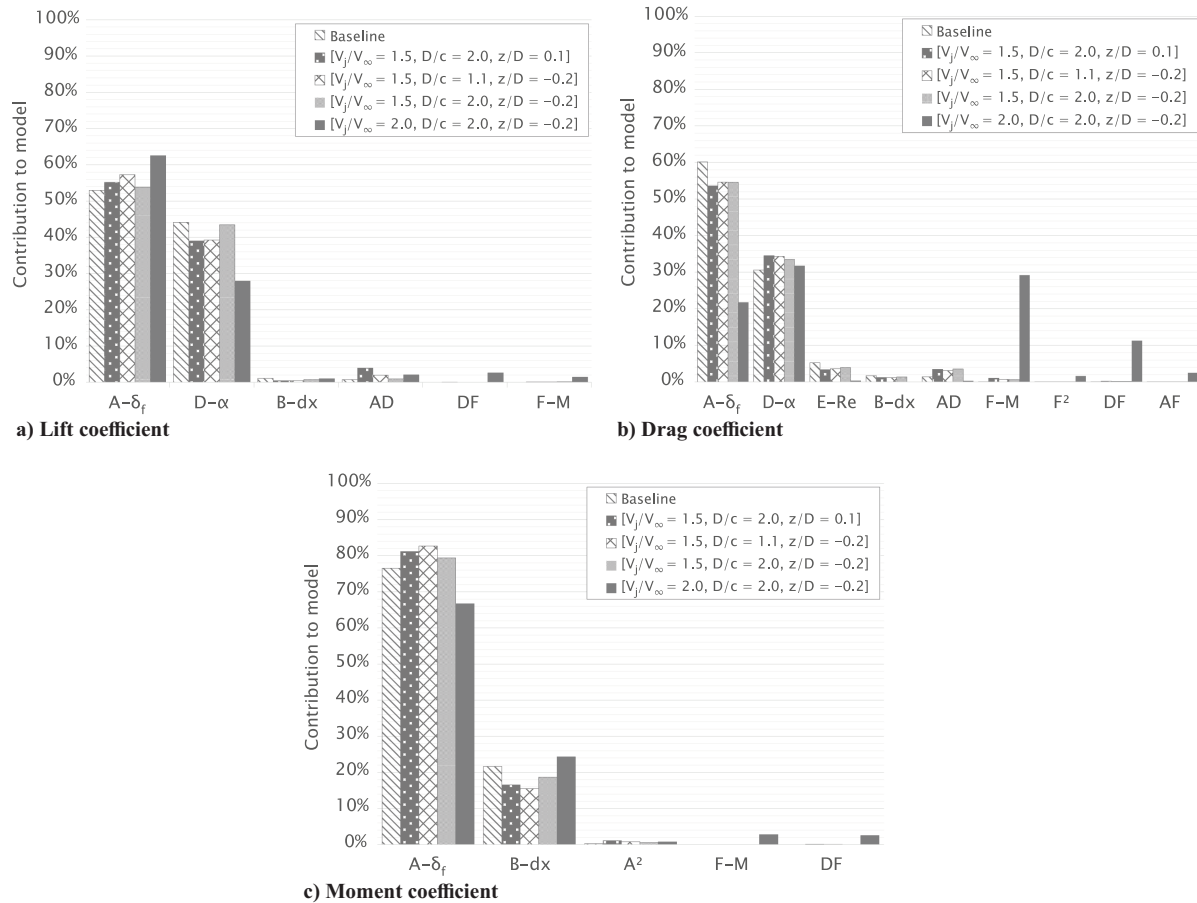
Fig. 9 Factor contributions to the lift, drag, and moment responses for the baseline model.

a) Lift coefficient

b) Drag coefficient

c) Moment coefficient

Fig. 11   Comparison of the relative contribution to the model with and without jet. Only terms with a contribution above 0.5% are shown.

Table 4   Summary of subset jet settings

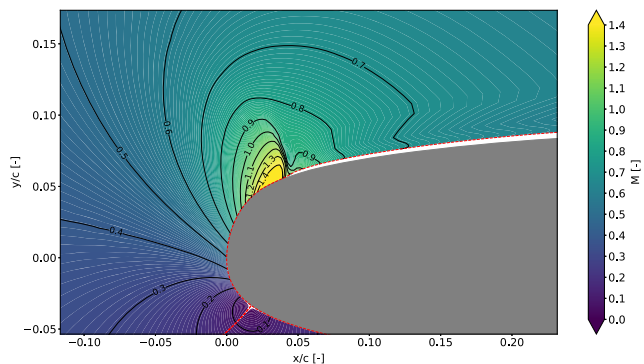| Subset	V_j/V_∞	D/c	z/D
1	1.5	2.0	0.1
2	1.5	1.1	−0.2
3	1.5	2.0	−0.2
4	2.0	2.0	−0.2

Fig. 12   Mach contour of the flowfield of an example run from subset 4, showing the shock on the main element and associated increase in displacement thickness (red dashed line).

space. Only model terms that contribute more than 0.5% to the total variability in the response are shown. It is clear that jet velocity ratio V_j/V_∞ (factor F) is the most dominant factor for all aerodynamic coefficients. Only varying V_j/V_∞ and keeping all other terms in

the model constant accounts for around 55% of the variation in lift across the design space. For drag and moment coefficients, this is 50 and 45%, respectively. Further dominant factors include angle of attack α (factor G), flap deflection angle δ_f (factor A), and diameter-to-chord ratio D/c (factor E). The latter contributes primarily to the lift and moment responses, and not as much to the drag responses.

Figure 14 displays the perturbation plots around the centerpoint, showing how factors affect the responses. Increasing the jet velocity ratio increases both lift and drag coefficients while decreasing the moment coefficient. While the lift and moment coefficients behave (nearly) linearly, the drag coefficient increases nonlinearly with an increasing jet velocity ratio. The linear scaling of C_l and C_m with V_j/V_∞ is readily explained by the fact that they are normalized by the freestream instead of the jet velocity. The same would be expected for C_d in fully incompressible conditions. However, we have already established that a portion of the design space contains significant transonic flow effects. Across the full jet design space, transonic flow occurs in about 25% of the design points, resulting in a nonlinear relation of C_d with both V_j/V_∞ and M. This becomes evident from Fig. 15, showing the interaction between V_j/V_∞ and M for the drag response. For low M, the drag coefficient scales linearly with V_j/V_∞, while for high M it becomes nonlinear. Figure 16 presents Mach contour plots for the two design points indicated in Fig. 15, showing the transonic region for the high M configuration. Table 5 contains a drag breakdown for both configurations shown in Fig. 16, showing that wave drag contributes nearly one-third to the total drag coefficient for the high M case.

Figure 15 also demonstrates that a relatively small contribution to the total model variability does not necessarily mean it is negligible in terms of the absolute response value. Although the $V_j/V_\infty - M$ interaction only contributes a few percent to the model, the change in drag coefficient varies between roughly 0.03 and 0.1 due to the

a) Lift coefficient   **b) Drag coefficient**   **c) Moment coefficient**
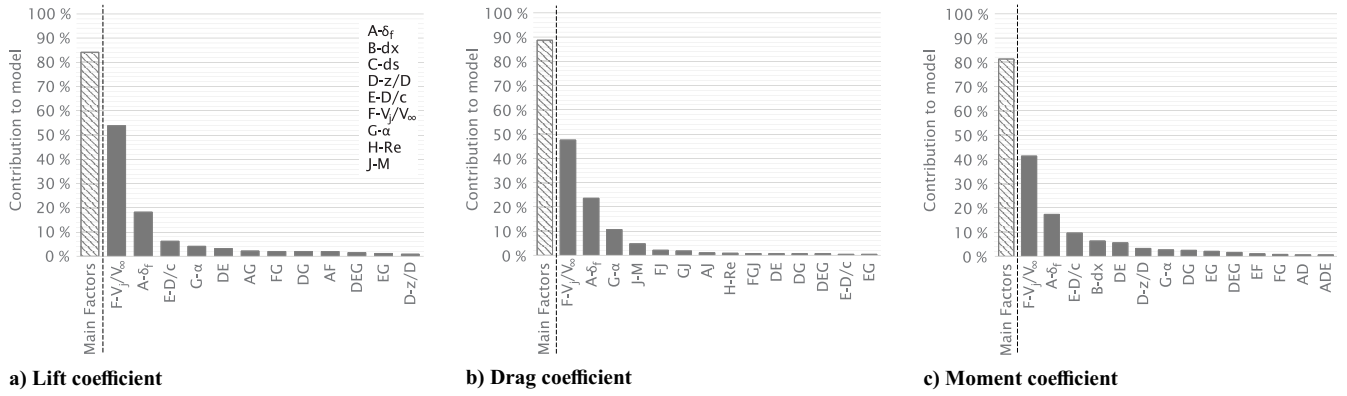
Fig. 13   Relative contribution of terms to the lift, drag, and moment responses. Only shows terms with a contribution $\geq 0.5\%$. Dashed bar indicates sum of main factors only.

a) Lift coefficient   **b) Drag coefficient**   **c) Moment coefficient**
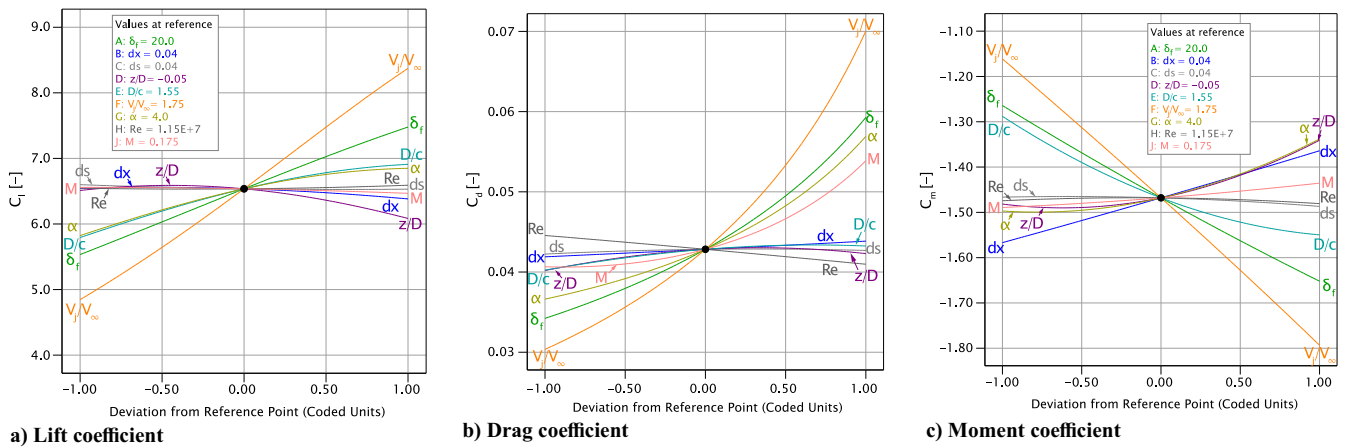
Fig. 14   Perturbation plots of the responses around the centerpoint of the full design, showing how the responses change when each factor is changed independently between their low (-1) and high (+1) value.
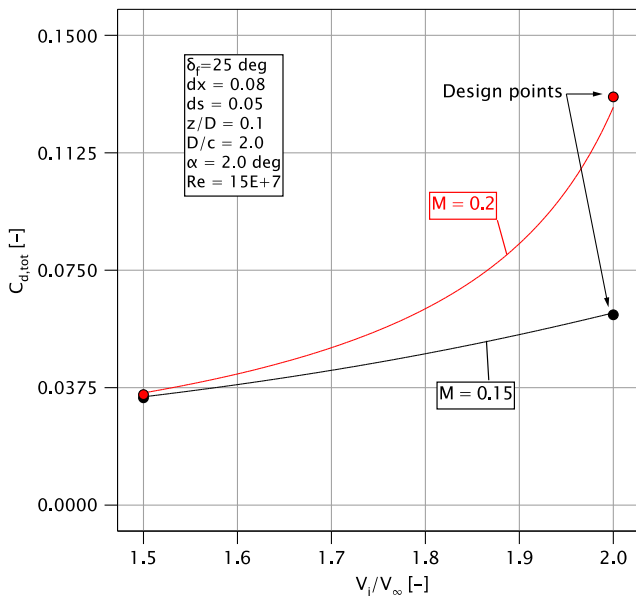

Fig. 15 C_d versus V_j/V_∞ for high and low M.

interaction. The presence of V_j/V_∞ in the model thus obscures the significance of other factors and interactions due to it having a disproportional impact on the responses. It is thus important to visualize the interactions and analyze how they affect the relationship between factors and responses.

1. Important Interactions in the Jet Design Space

From the summed contribution of all main factors (the dashed bars in Fig. 13), we see that, compared to the baseline design, a significant portion depends on interactions. For the lift coefficient, roughly 15% of the response depends on interactions, while for the drag and moment coefficients, this is 10 and 23%, respectively. The most important interactions can be split into two sets. For lift and moment coefficients, the main interactions involve δ_f (A), z/D (D), D/c (E), α (G), and V_j/V_∞ (F). For the drag coefficient, a second set of important interactions exists between α (G), V_j/V_∞ (F), δ_f (A), and M (J). The latter set of interactions can again be attributed to transonic flow conditions mentioned previously. The maximum velocity in the domain is mostly dictated by the upstream velocity (i.e., V_j/V_∞ and M) and the streamline curvature (i.e., α and δ_f). We can therefore attribute the contributions of interactions FJ ($V_j/V_\infty - M$), GJ ($\alpha - M$), AJ ($\delta_f - M$), and FGJ ($V_j/V_\infty - \alpha - M$) to the occurrence of transonic flow in the design space.

The other set of interactions i.e., between δ_f (A), z/D (D), D/c (E), α (G), and V_j/V_∞ (F) can again be split into two groups. The first group consists of interactions between α, δ_f, and V_j/V_∞. They are visualized through the lift response surface in Fig. 17. An interaction means that the response curve of one factor changes when another factor is changed. The edges of the response surfaces are projected on the vertical planes to make this more visible. Slight interaction effects are visible, where for higher V_j/V_∞ the lift response becomes nonlinear with α and steeper with δ_f. However, the effects of these interactions are small compared to the impact of the jet velocity ratio itself.
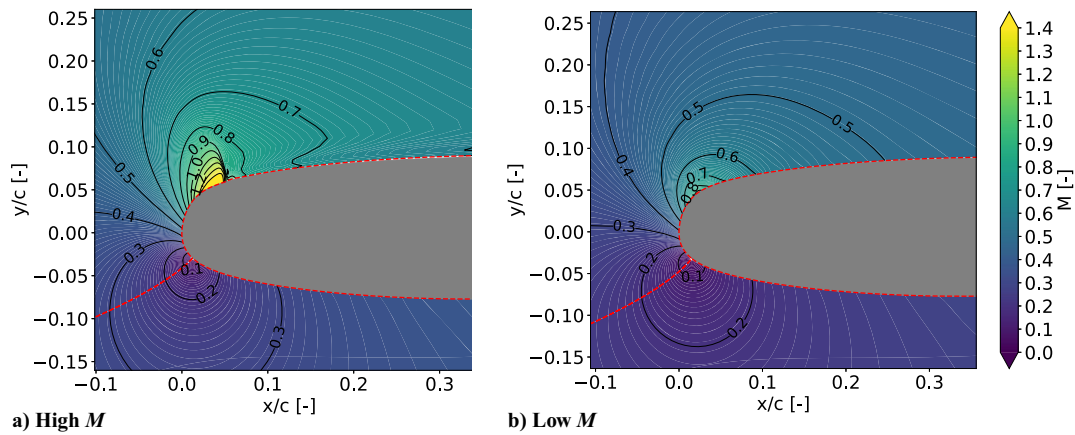
Fig. 16   Mach contours for low and high Mach number settings, showing transonic conditions; α set to low, other factors to high.

Table 5   Drag coefficient breakdown showing impact of wave drag

V_j/V_∞	M_∞	M_{max}	$C_{d,tot}$	$C_{d,v}$	$C_{d,w}$
2	0.15	0.957	0.0608	0.0	0.0608
2	0.2	1.585	0.1305	0.0883	0.0422

The second group features factors α (G), z/D (D), and D/c (E). Figure 18 shows the response surface of the lift coefficient for z/D and D/c for various levels of α, with all other factors at the center-point value. Two-factor interactions, such as $z/D - D/c$ (DE), are illustrated by the significant change in slope in the projections on the vertical planes. We can see that the response surface shape changes significantly for different α, a result from the interactions $D/c - \alpha$ (EG), $z/D - \alpha$ (DG), and $z/D - D/c - \alpha$ (DEG). Unlike the interactions with V_j/V_∞, the impact of this group of interactions is in the order of magnitude of the impact of the factors on their own. The jet position z/D particularly does not contribute much to the lift response by itself but drastically changes the response to D/c.

The response surfaces show that a small jet generates more lift at a lower position, while a larger jet benefits from a higher position. However, the impact of vertical position on the lift response with a small jet is generally larger than for a large jet, particularly at higher angles of attack. At low α, a higher position z/D is always beneficial to lift, while at higher α this fully inverts and a lower z/D yields a higher lift coefficient for any D/c. For an explanation, we look at the

immersion of the flap. Ting et al. [24] already showed that the lift of a single airfoil immersed in a jet depends on the ratio between jet height and airfoil chord. Relatively large ratios are necessary to get the full effect of the additional velocity within the jet. In the present study, the jet passes the airfoil mostly on the suction side, as its trajectory is affected by the angle of attack and circulation on the airfoil.

Figure 19 illustrates how the flap immersion is a function of the interaction of D/c and z/D by visualizing the jet edge for various configurations. The pressure distributions of these configurations are displayed in Fig. 20, while Table 6 presents a lift breakdown. For a small jet, the lower jet edge approaches the flap very closely; in the case of Fig. 19b, it even travels over the flap. This drastically reduces the flap lift, which in turn affects the main element lift. For the larger jet, the lower jet edge travels well below the flap for both vertical positions, with little change in lift or pressure distribution as a result. It is easy to imagine how this will be further affected by α, due to its effect on lift and thus upwash. Overall, the interactions between α, z/D, and D/c suggest that a high position is generally beneficial to the lift coefficient, on the condition that the flap is sufficiently immersed.

2.   Lift Response Separated by Element

To further investigate the interactions in the jet design space with the flap immersion and its effect on the lift response, we investigate models based on the main element and flap element lift responses separately. The factor contributions for these models are shown in Fig. 21 and compared to the total lift model. The factor contributions
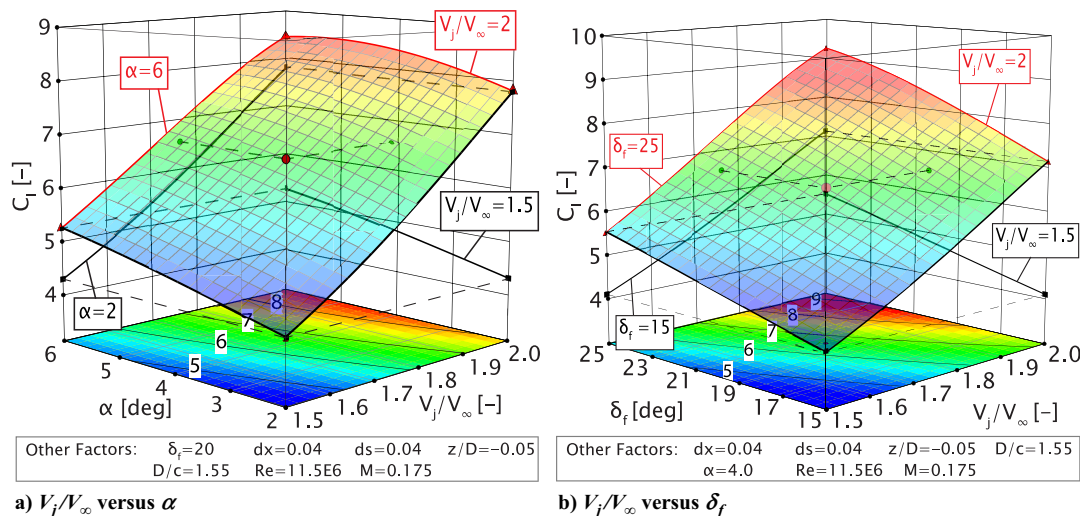

Fig. 17   Response surfaces of the lift coefficient for the two main interactions involving V_j/V_∞. All other factors are set to the centerpoint. Vertical planes show projections of the edges of the surface.
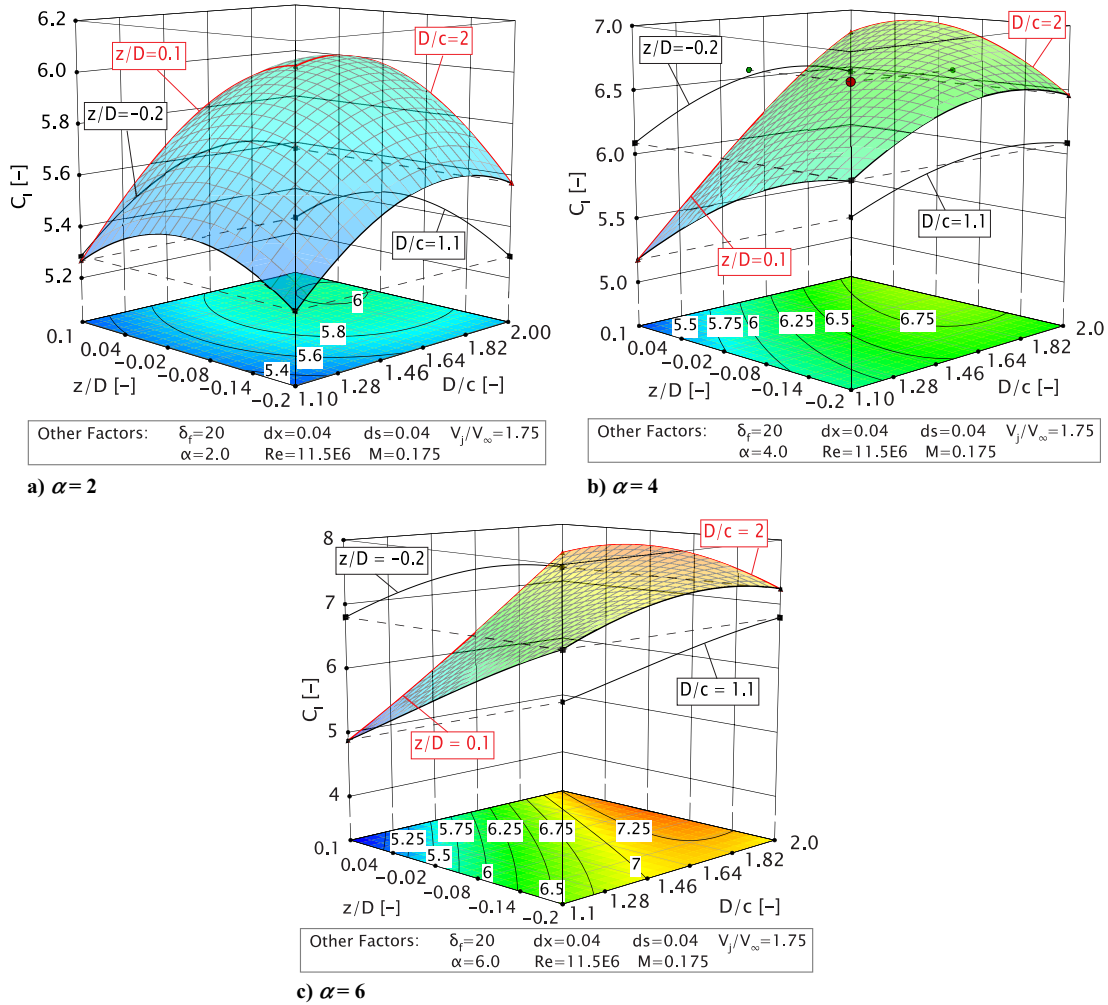
Fig. 18 Response surfaces of the lift coefficient for the interaction of D/c and z/D for various settings of α and all other factors set to the centerpoint. Vertical planes show projections of the edged of the surface.

for main element lift are very similar to the total lift coefficient. The jet velocity ratio is dominant, and the large contribution of the flap deflection underlines the interactive effect between both elements. However, contributions to the flap lift response deviate from the total and main element lift responses. The contribution of V_j/V_∞ is more than halved, as are its interactions. Contributions of α are much lower than for the main element lift. The flap lift coefficient is more dependent on D/c, z/D, and interactions between D/c, z/D, and α. In fact, the contribution of D/c, z/D, and α—which are dominant in the trajectory of the jet—together contribute more to the model variability than V_j/V_∞.

Figure 22 shows the perturbation plots for the flap lift response at different settings of α (all other factors set to the centerpoint). For low angles of attack, z/D and D/c have a relatively minor effect on flap lift coefficient and are optimal around the centerpoint. As α increases, however, the impact of z/D and D/c increases due to their interactions with α. The optimum for flap lift coefficient shifts to lower z/D and higher D/c, and the influence of these factors exceeds that of the jet velocity ratio.

The flap lift response is thus mostly dependent on factors that affect the jet trajectory and how much of the jet passes through each side of the airfoil. Furthermore, the perturbation plots show that an optimum for z/D and D/c exists within the design space. This aligns with the conclusion that the flap requires a minimum immersion in the jet. As α is increased, this optimum shifts to lower z/D or higher D/c. After minimum immersion of the flap is reached, a larger jet or a lower position no longer benefits the flap lift response, and more lift is achieved by increasing the extent of the jet on the suction side of the airfoil. This follows standard circulation theory, where additional dynamic pressure on

the suction side should increase airfoil circulation. Unfortunately, we cannot determine the exact relationship of required immersion for the flap from the current dataset. The CCD only contains two different jet positions for each combination of all other factors, so it does not include the flowfield data to investigate systematically marching the jet edge closer to the flap. This will therefore be left to future research.

C. Lift Augmentation

The final response of interest is the lift augmentation factor, defined as $K_{C_l} = (C_{l,\text{jet flow}}/C_{l,\text{uniform flow}})$. This quantifies how much the presence of the jet in the flowfield augments the lift response compared to the equivalent baseline configuration. Figure 23a shows the factors contributing to the lift augmentation factor. The lift augmentation is clearly dominated by V_j/V_∞, which contribute nearly 70% to the response variability. The remaining 30% are mostly a function of D/c, z/D, α, and their interactions. The perturbation of K_{C_l} about the centerpoint is given in Fig. 23b, showing that K_{C_l} increases linearly with V_j/V_∞.

The perturbation curves for D/c, z/D, and α are similar to those for the flap lift response. We have shown that the total lift response is significantly affected by these factors and their interactions, which is attributed to their impact on the flap lift more than the main element lift. Of all simulations, the configurations that yield the maximum $C_{l,\text{total}}$ are mostly also the configurations yielding maximum $C_{l,\text{main}}$, but not with maximum K_{C_l}. The latter is more strongly correlated with maximum $C_{l,\text{flap}}$. We can therefore conclude that for a given jet velocity ratio, the flap immersion is critical to the achieved lift augmentation.

a) $D/c = 1.1$ (low), $z/D = -0.2$ (low)

b) $D/c = 1.1$ (low), $z/D = 0.2$ (high)

c) $D/c = 2$ (high), $z/D = -0.2$ (low)

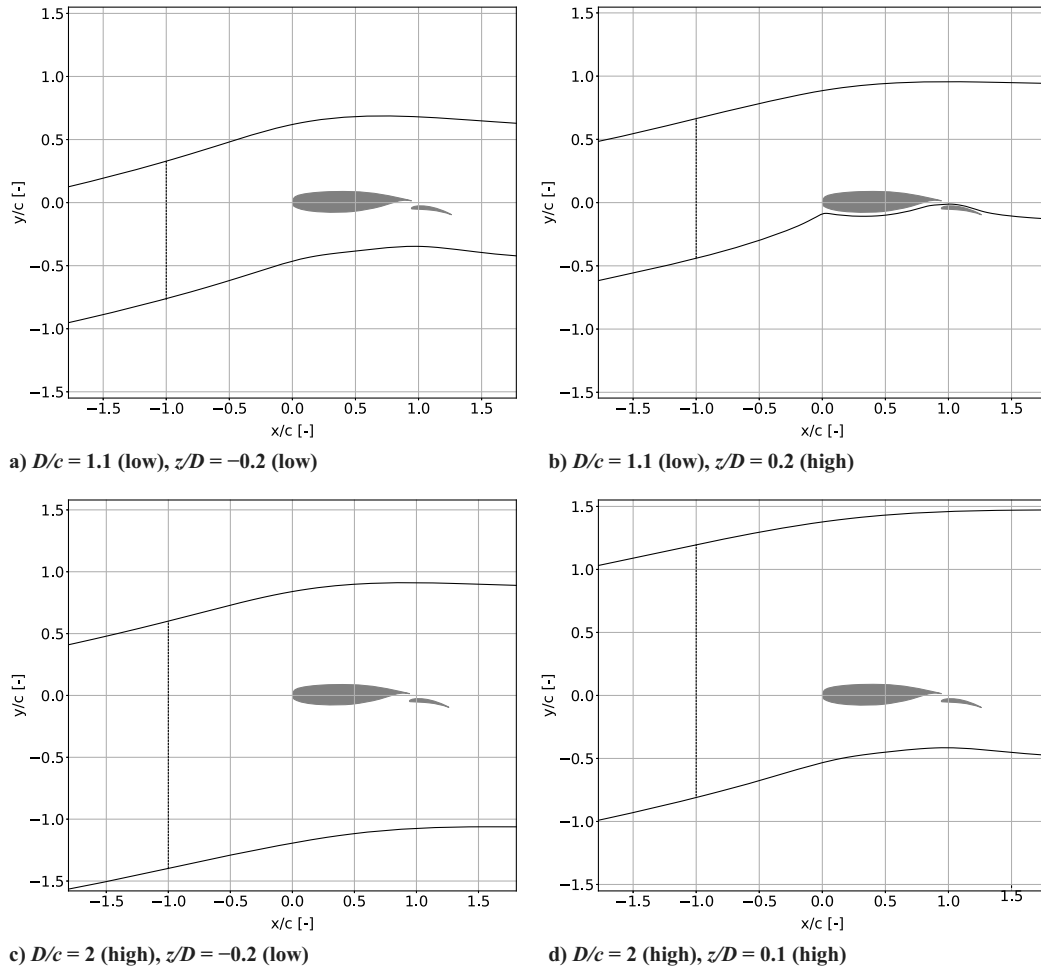d) $D/c = 2$ (high), $z/D = 0.1$ (high)

Fig. 19   Visualization of the jet trajectory for various D/c and z/D. From MSES simulations. Jet constraint indicated by dashed line. Other factor values: $V_j/V_\infty = 1.5, \alpha = 6, \delta_f = 15, dx = 0, ds = 0.05, Re = 15e6, M = 0.15$.
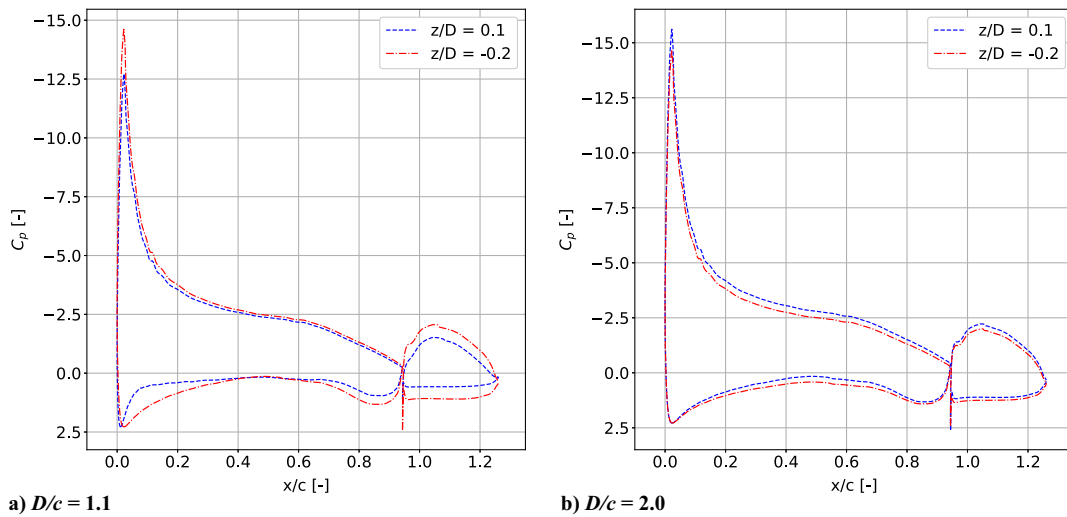

a) $D/c = 1.1$

b) $D/c = 2.0$

Fig. 20   Pressure distributions showing the effect of vertical jet position for small and large jet sizes.

Table 6   Lift coefficient breakdown showing impact of jet position for different jet sizes

D/c	z/D	$C_{l,\text{tot}}$	$C_{l,\text{main}}$	$C_{l,\text{flap}}$
1.1	0.1	3.666	3.223	0.440
1.1	−0.2	4.451	3.706	0.745
2	0.1	4.840	4.053	0.787
2	−0.2	3.915	3.915	0.770

D.   Reflections on Propeller–Wing–Flap Systems

The purpose of this paper is to improve the understanding of propeller–wing–flap aerodynamic interactions by studying simplified representations of the system. We therefore reflect on the findings in this study and how they impact propeller–wing–flap systems. This discussion is, of course, limited to the increase in dynamic pressure that is present in the slipstream and cannot account for the many three-dimensional effects such as swirl and
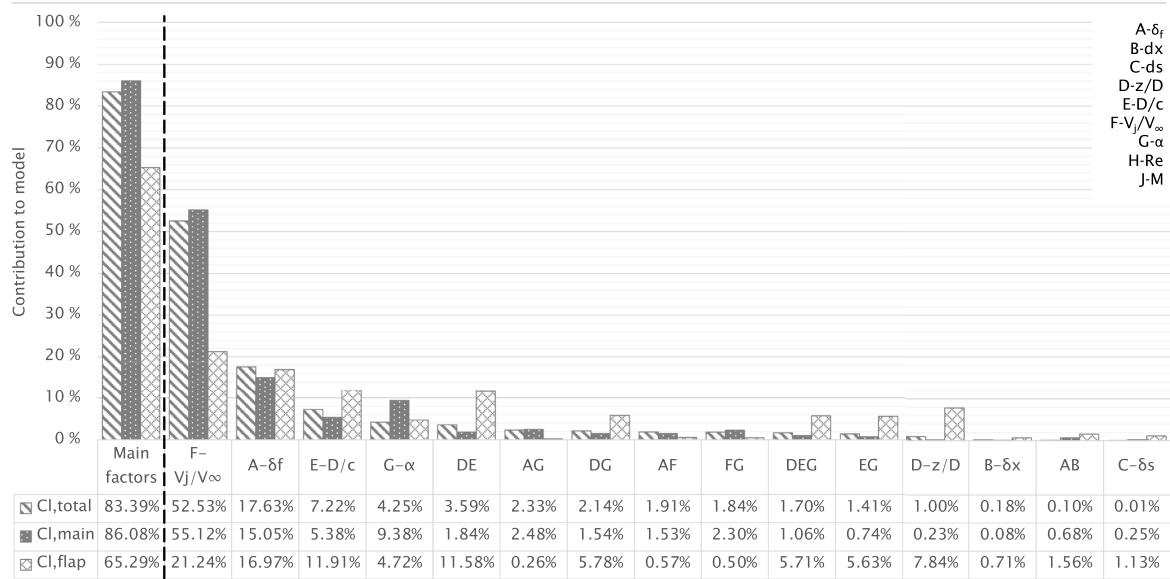
Fig. 21   Comparison of dominance of terms to lift response of total airfoil, main, and flap element. Summed contributions of all main factors (no interactions) are shown left of the dashed line; individual contributions reported to the right.

	Main factors	F–Vj/V∞	A–δf	E–D/c	G–α	DE	AG	DG	AF	FG	DEG	EG	D–z/D	B–δx	AB	C–δs
Cl,total	83.39%	52.53%	17.63%	7.22%	4.25%	3.59%	2.33%	2.14%	1.91%	1.84%	1.70%	1.41%	1.00%	0.18%	0.10%	0.01%
Cl,main	86.08%	55.12%	15.05%	5.38%	9.38%	1.84%	2.48%	1.54%	1.53%	2.30%	1.06%	0.74%	0.23%	0.08%	0.68%	0.25%
Cl,flap	65.29%	21.24%	16.97%	11.91%	4.72%	11.58%	0.26%	5.78%	0.57%	0.50%	5.71%	5.63%	7.84%	0.71%	1.56%	1.13%

a) $\alpha = 2$ *deg*

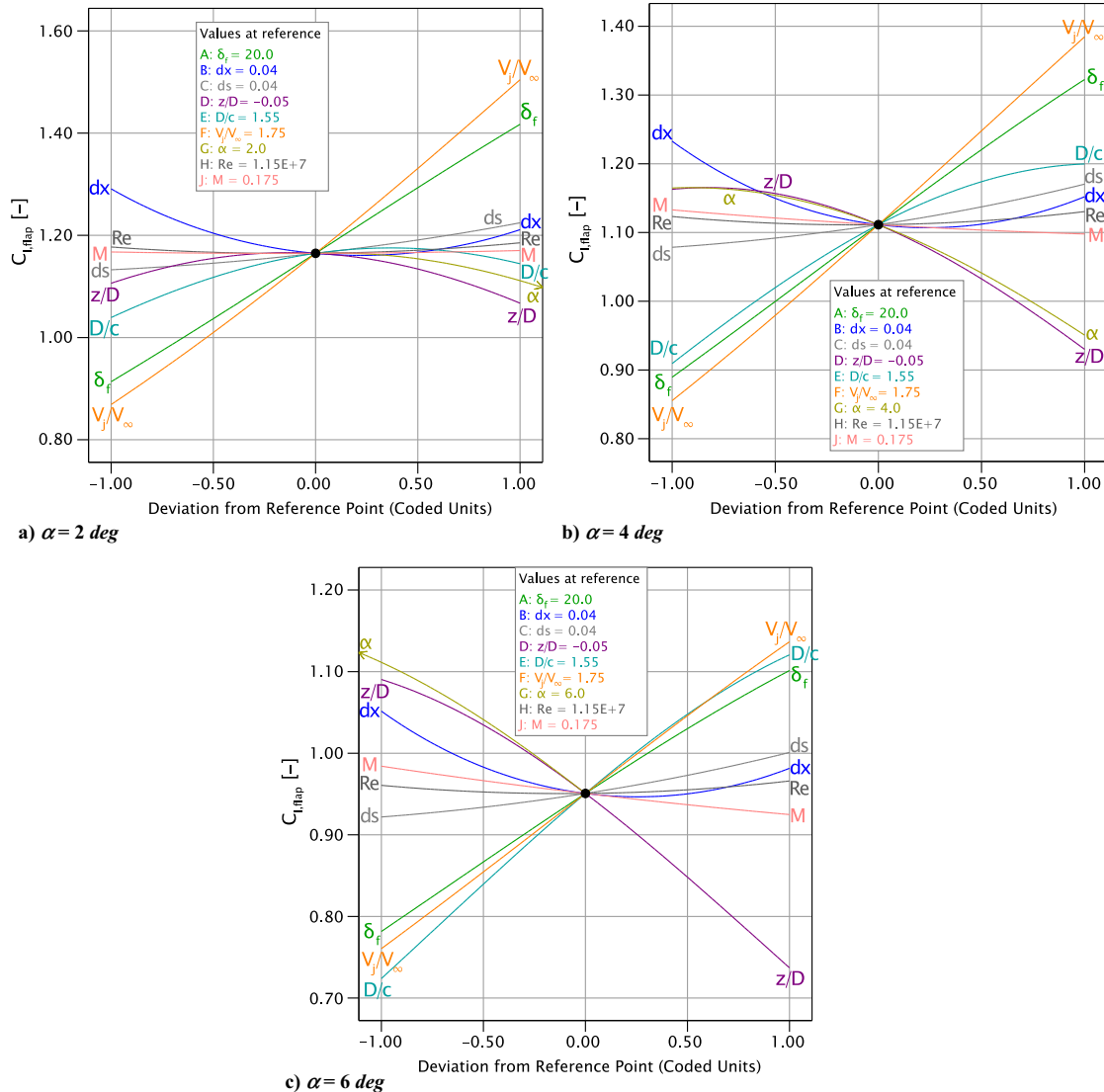

b) $\alpha = 4$ *deg*

c) $\alpha = 6$ *deg*

Fig. 22   Perturbation of flap lift coefficient by main factors at different angles of attack. Other factors are set to the centerpoint value. Coded units refer to the low (−1) and high (+1) values in the CCD.
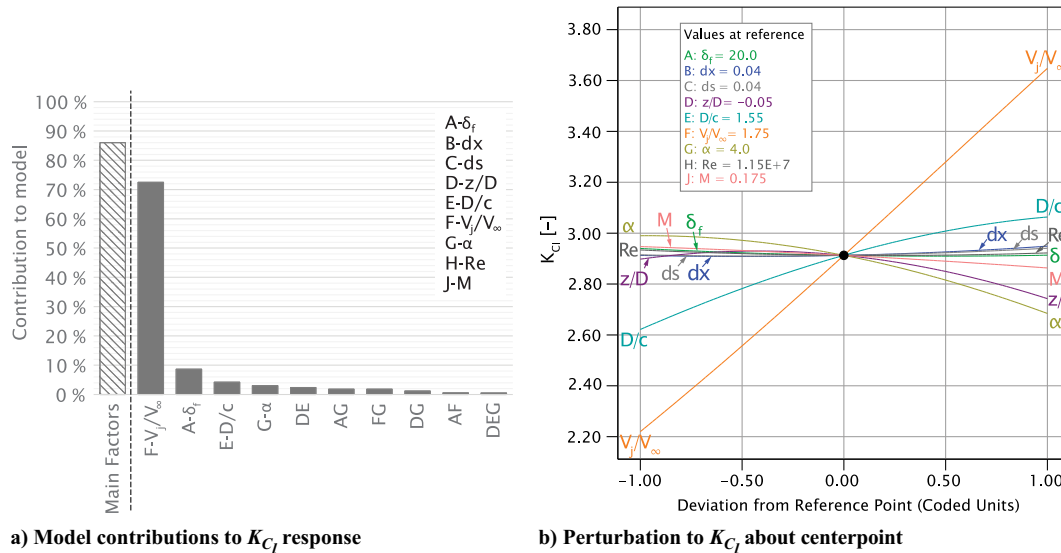
a) **Model contributions to K_{C_l} response**

b) **Perturbation to K_{C_l} about centerpoint**

Fig. 23 Model contribution summary and perturbation plot of the metamodel for lift augmentation factor K_{C_l}.

tip vortex–wing interactions. Nonetheless, under the assumption that the dynamic pressure is the dominant parameter in the effect of the slipstream on the wing lift, we can make several recommendations based on the simplified representations of the system.

The analyses in this paper emphasize the importance of the alignment of the slipstream (or jet) with the airfoil. The particular trajectory of the slipstream over the airfoil is a function of the relative position, the angle of attack, and the wing circulation. In traditional propeller–wing interaction research in the cruise regime, the longitudinal position of the propeller relative to the wing is often neglected, based on Munk's stagger theorem and small angle assumption [8]. For high angles of attack or high wing circulation, however, this longitudinal distance cannot be overlooked. It should be noted that the jet in this paper is formed far ahead of the airfoil and thus does not account for the effect of the incidence angle of the propeller and how it redirects the flow. For highly loaded propellers, the local redirection of the flow may end up dominating the trajectory of the slipstream.

The importance of the flap immersion also highlights the impact of slipstream deformation on lift augmentation by propeller blowing. In previous work [18], the authors showed how the immersion of the main element and flap are strongly affected by slipstream deformation, particularly in high-lift conditions. Based on the findings in this paper, the local lift augmentation can be expected to vary strongly in the spanwise direction as a result of the varying wing immersion.

Finally, the current state-of-the-art in propeller–wing–flap interaction studies generally accepts that a lower position of the propeller is more beneficial for lift augmentation (e.g., [12]). This general rule is confirmed by the presented results when D/c is small and only the dynamic pressure increase is considered. However, the results in this paper also suggest that this could change for larger D/c, assuming that it is not dominated by the effects of other slipstream characteristics.

V. Conclusions

We investigated the impact of a jet of higher dynamic pressure on the aerodynamic performance of a two-dimensional multi-element airfoil. We simulated a wide range of configurations that varied nine different factors, which together controlled jet and freestream velocity, jet position, and flap position. We quantified which of these factors and interactions between factors are dominant with respect to lift, drag, and moment coefficient, finding that the jet velocity ratio is dominant for all of the responses. We have shown that the jet can induce transonic flow regions on the main element, which severely affect the aerodynamic responses, in particular, the drag coefficient.

In the absence of critical Mach numbers, the factor dependency is comparable to uniform flow conditions, showing the aerodynamic behavior of multi-element airfoils is not fundamentally affected by the presence of the jet.

We furthermore investigated the interactions between jet size D/c, jet position z/D, and angle of attack α. We established that these interactions influence the jet alignment with the airfoil and how much the flap is immersed in the flow. The optimal position of the jet with respect to the airfoil is found to change between smaller jets, which benefit from lower positions, and larger jets, which generally favor higher positions. We quantified the dominant factors and interactions for the main element and flap lift coefficients separately, concluding that the impact of D/c, z/D, α, and their interactions stems mostly from their influence on the flap lift. We conclude that a minimum flap immersion is critical to the lift augmentation resulting from the jet, after which passing the jet over the suction side of the airfoil yields the most impact on lift coefficient.

The conclusions from this paper can help to further understand the complex aerodynamic interactions of propeller–wing–flap systems by providing insight into how the wing is affected by the high dynamic pressure in the propeller slipstream. Although highly geometry-specific, the induction of shocks is an important consideration that cannot be overlooked in high-lift applications of propeller–wing integration. This paper furthermore emphasizes the importance of the deformation of the slipstream and its alignment with the wing, aspects that are currently still poorly understood in the field of propeller–wing interaction in high-lift conditions.
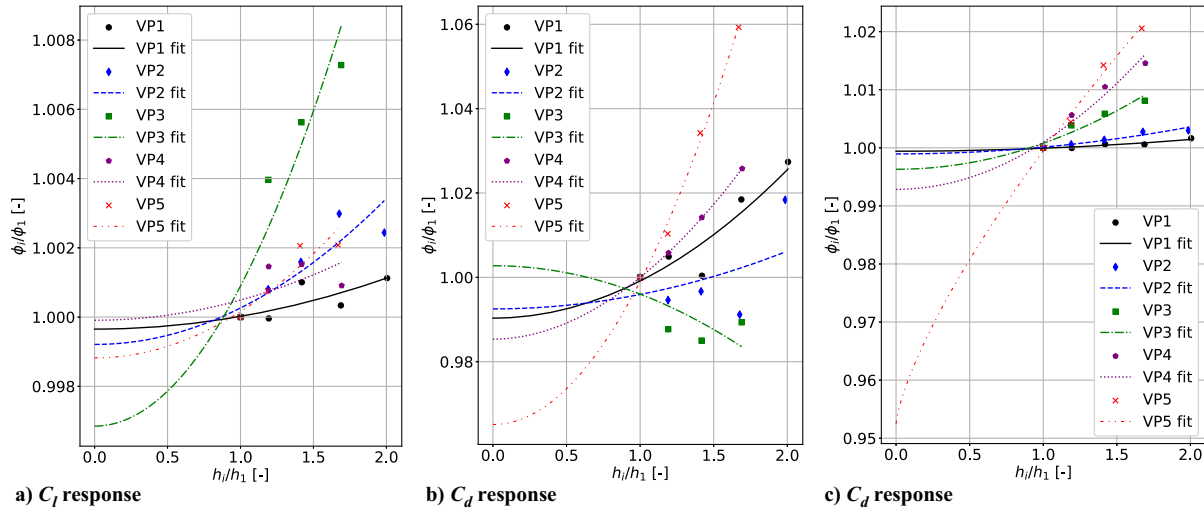
Appendix: RANS Grid Convergence Study

For each of the VPs evaluated in Sec. III, we carried out a grid convergence study following the approach outlined by Eça and Hoekstra [33] to estimate the discretization error. This approach uses least-squares-based Richardson extrapolation to deal with the inherent scatter present in simulations on unstructured meshes and incorporate this into the error estimation. Table A1 summarizes the number

Table A2 Discretization error for the finest grid of each verification point

Parameter	VP1 (Max L/D)	VP2 (Min C_d)	VP3 (Max C_l)	VP4 (Max C_d)	VP5 (Min L/D)
N_{grids}	5	5	4	4	4
C_l	0.36%	0.37%	1.33%	0.24%	0.43%
C_d	3.07%	1.81%	1.55%	1.84%	4.49%
C_m	0.18%	0.38%	1.45%	2.54%	6.02%

Table A1   Overview of number of cells and relative cell sizes for each configuration

	VP1 (Max L/D)		VP2 (Min C_d)		VP3 (Max C_l)		VP4 (Max C_d)		VP5 (Min L/D)	
Grid	N_{cells}	h_i/h_1	N_{cells}	h_i/h_1	N_{cells}	h_i/h_1	N_{cells}	h_i/h_1	N_{cells}	h_i/h_1
1	$4.14e6$	2.01	$3.28e6$	1.99	—	—	—	—	—	—
2	$5.85e6$	1.69	$4.60e6$	1.68	$6.03e6$	1.69	$5.79e6$	1.69	$3.59e6$	1.67
3	$8.26e6$	1.42	$6.47e6$	1.41	$8.57e6$	1.42	$8.25e6$	1.42	$5.04e6$	1.41
4	$1.17e7$	1.19	$9.14e6$	1.19	$1.21e7$	1.19	$1.17e7$	1.19	$7.10e6$	1.19
5	$1.67e7$	1.00	$1.29e7$	1.00	$1.72e7$	1.00	$1.66e7$	1.00	$1.00e7$	1.00

a) C_l response   b) C_d response   c) C_d response

Fig. A1   Grid convergence trends for lift, drag, and moment coefficients of the airfoil for each of the verification runs.

of cells and relative average cell size in each grid for each run. The various mesh refinements were achieved by reducing the main airfoil element size by 1.2, which results in consistently increasing refinement for each consecutive grid due to the dependency on the main airfoil discretization. Only the initial layer height and number of inflation layers remain constant between each refinement to satisfy the observation by Roache [34] that grid convergence should be performed from the edge of the wall layer out. The total number of cells varies between VPs due to differences in the inflation layers, which are Reynolds number dependent, and different jet positions.

Table A2 shows the discretization error of the finest grid of each VP resulting from the grid convergence study. Verification points 3–5 were not properly converged for the coarsest grids, so the convergence for these points is only based on the four finest grids. The resulting discretization error is below 5% for all coefficients, except for the moment coefficient of VP 5. We attribute this to the grids not being in the asymptotic region, resulting in unpredictable behavior of the least-squares Richardson extrapolation as shown in Fig. A1. The maximum difference in C_m between all grids of VP5 is within 2% of each other, which we deem sufficient for a comparison with MSES. The comparisons in this paper are all based on the finest grids of the convergence study.

References

[1] Moore, M. D., and Fredericks, B., "Misconceptions of Electric Aircraft and Their Emerging Aviation Markets," *52nd Aerospace Sciences Meeting*, AIAA Paper 2014-0535, 2014.
https://doi.org/10.2514/6.2014-0535

[2] Kuhn, R. E., and Draper, J. W., "An Investigation of a Wing-Propeller Configuration Employing Large-Chord Plain Flaps and Large-Diameter Propellers for Low-Speed Flight and Vertical Take-Off," NACA TN 3307, 1954.

[3] Viken, J. K., Viken, S., Deere, K. A., and Carter, M., "Design of the Cruise and Flap Airfoil for the X-57 Maxwell Distributed Electric Propulsion Aircraft," *35th AIAA Applied Aerodynamics Conference*, AIAA Paper 2017-3922, 2017.
https://doi.org/10.2514/6.2017-3922

[4] Stoll, A. M., Bevirt, J., Moore, M. D., Fredericks, W. J., and Borer, N. K., "Drag Reduction Through Distributed Electric Propulsion," *14th AIAA Aviation Technology, Integration, and Operations Conference*, AIAA, Reston, VA, 2014, pp. 16–20.
https://doi.org/10.2514/6.2014-2851

[5] Jameson, A., "The Analysis of Propeller-Wing Flow Interaction," *Analytic Methods in Aircraft Aerodynamics*, NASA Special Publications 228, Langley, 1970, pp. 721–742.

[6] Kroo, I., "Propeller-Wing Integration for Minimum Induced Loss," *Journal of Aircraft*, Vol. 23, No. 7, 1986, pp. 561–565.
https://doi.org/10.2514/3.45344

[7] Witkowski, D. P., Lee, A. K., and Sullivan, J. P., "Aerodynamic Interaction Between Propellers and Wings," *Journal of Aircraft*, Vol. 26, No. 9, 1989, pp. 829–836.
https://doi.org/10.2514/3.45848

[8] Veldhuis, L., "Propeller Wing Aerodynamic Interference," Ph.D. Dissertation, Delft Univ. of Technology, Delft, The Netherlands, 2005, http://www.narcis.nl/publication/RecordID/oai:tudelft.nl:uuid:8ffbde9c-b483-40de-90e0-97095202fbe3.

[9] Agrawal, D. R., Asad, F., Berk, B., Long, T., Lubin, J., Courtin, C., Drela, M., Hansman, R. J., and Thomas, J., "Wind Tunnel Testing of a Blown Flap Wing," *AIAA Aviation Forum*, AIAA Paper 2019-3170, 2019.
https://doi.org/10.2514/6.2019-3170

[10] Long, T., Drela, M., Hansman, J., and Courtin, C., "Parametric Design Study for a Blown Flapped Wing," *AIAA Aviation 2021 Forum*, AIAA Paper 2021-2871, 2021.
https://doi.org/10.2514/6.2021-2871

[11] Keller, D., "Towards Higher Aerodynamic Efficiency of Propeller-Driven Aircraft with Distributed Propulsion," *CEAS Aeronautical Journal*, Vol. 12, No. 4, 2021, pp. 777–791.
https://doi.org/10.1007/s13272-021-00535-5

[12] Firnhaber Beckers, M., Schollenberger, M., Lutz, T., Bongen, D., Radespiel, R., Florenciano, J. L., and Funes-Sebastian, D. E., "CFD Investigation of High-Lift Propeller Positions for a Distributed Propulsion System," *AIAA Aviation 2022 Forum*, AIAA Paper 2022-3217, 2022.
https://doi.org/10.2514/6.2022-3217

[13] Smith, A. M. O., "High-Lift Aerodynamics," *Journal of Aircraft*, Vol. 12, No. 6, 1975, pp. 501–530.
https://doi.org/10.2514/3.59830

[14] Kuhn, R. E., and Draper, J. W., "Investigation of Effectiveness of Large-Chord Slotted Flaps in Deflecting Propeller Slipstreams Downward for Vertical Take-Off and Low-Speed Flight," NACA TN 3364, 1955.

[15] Kuhn, R. E., "Investigation of the Effects of Ground Proximity and Propeller Position on the Effectiveness of a Wing with Large-Chord Slotted Flaps in Redirecting Propeller Slipstreams Downward for Vertical Take-Off," NACA TN 3629, 1956.

[16] Kuhn, R. E., "Semiempirical Procedure for Estimating Lift and Drag Characteristics of Propeller-Wing-Flap Configurations for Vertical- and Short-Take-Off-and-Landing Airplanes," NASA TM 1-16-59L, 1959, http://ntrs.nasa.gov/archive/nasa/casi.ntrs.nasa.gov/19980232082.pdf

[17] James, H. A., Wingrove, R. C., Hoiznauser, C. A., and Drinkwater III, F. J., "Wind-Tunnel and Piloted Flight Simulator Investigation of a Deflected-Slipstream VTOL Airplane, the Ryan VZ-3RY," NASA TN D-89, 1959.

[18] Duivenvoorden, R., Suard, N., Sinnige, T., and Veldhuis, L. L., "Experimental Investigation of Aerodynamic Interactions of a Wing with Deployed Fowler Flap under Influence of a Propeller Slipstream," *AIAA Aviation 2022 Forum*, AIAA Paper 2022-3216, 2022, pp. 1–19.
https://doi.org/10.2514/6.2022-3216

[19] Drela, M., "Newton Solution of Coupled Viscous/Inviscid Multielement Airfoil Flows," *AIAA 21st Fluid Dynamics, Plasma Dynamics and Lasers Conference*, AIAA Paper 1990-1470, 1990.
https://doi.org/10.2514/6.1990-1470

[20] Drela, M., "Design and Optimization Method for Multi-Element Airfoils," *AIAA/AHS/ASEE Aerospace Design Conference*, AIAA Paper 1993-0969, 1993.
https://doi.org/10.2514/6.1993-969

[21] Drela, M., "A User's Guide to MSES 3.05," MIT Department of Aeronautics and Astronautics, TR, Cambridge, MA, July 2007, https://web.mit.edu/drela/Public/web/mses/.

[22] van den Berg, B., and Oskam, B., "Boundary Layer Measurements on a Two-Dimensional Wing with Flap and a Comparison with Calculations," National Aerospace Lab. (NLR) MP 79034 U, Hague, The Netherlands, 1979.

[23] Montgomery, D. C., *Design and Analysis of Experiments*, 8th ed., Wiley, Hoboken, NJ, 2013, Chaps. 5–11.

[24] Ting, L., Liu, C. H., and Kleinstein, G., "Interference of Wing and Multipropellers," *AIAA Journal*, Vol. 10, No. 7, 1972, pp. 906–914.
https://doi.org/10.2514/3.50244

[25] Patterson, M. D., Derlaga, J. M., and Borer, N. K., "High-Lift Propeller System Configuration Selection for NASA's SCEPTOR Distributed Electric Propulsion Flight Demonstrator," *16th AIAA Aviation Technology, Integration, and Operations Conference*, AIAA Paper 2016-3922, June 2016.
https://doi.org/10.2514/6.2016-3922

[26] Landman, D., Simpson, J., Vicroy, D., and Parker, P., "Efficient Methods for Complex Aircraft Configuration Aerodynamic Characterization Using Response Surface Methodologies," *Collection of Technical Papers—44th AIAA Aerospace Sciences Meeting*, AIAA Paper 2006-0922, Jan. 2006.
https://doi.org/10.2514/6.2006-922

[27] O'Brien, R. M., "A Caution Regarding Rules of Thumb for Variance Inflation Factors," *Quality and Quantity*, Vol. 41, No. 5, 2007, pp. 673–690.
https://doi.org/10.1007/s11135-006-9018-6

[28] Daoud, J. I., "Multicollinearity and Regression Analysis," *Journal of Physics: Conference Series*, Vol. 949, No. 1, 2018, Paper 012009.
https://doi.org/10.1088/1742-6596/949/1/012009

[29] Baker, F. D., and Bargmann, R. E., "Orthogonal Central Composite Designs of the Third Order in the Evaluation of Sensitivity and Plant Growth Simulation Models," *Journal of the American Statistical Association*, Vol. 80, No. 391, 1985, pp. 574–579.
https://doi.org/10.1080/01621459.1985.10478156

[30] Zhang, T., Higgins, R. J., Qiao, G., and Barakos, G. N., "Optimization of Distributed Propulsion Using CFD," *AIAA Aviation 2022 Forum*, AIAA Paper 2022-3299, 2022.
https://doi.org/10.2514/6.2022-3299

[31] Yankam, B. M., and Oladugba, A. V., "Augmented Orthogonal Uniform Composite Designs for Fitting Third-Order Model," *Journal of Statistical Theory and Practice*, Vol. 16, No. 2, 2022, pp. 1–14.
https://doi.org/10.1007/s42519-022-00260-0

[32] Landman, D., Simpson, J., Mariani, R., Ortiz, F., and Britcher, C., "Hybrid Design for Aircraft Wind-Tunnel Testing Using Response Surface Methodologies," *Journal of Aircraft*, Vol. 44, No. 4, 2007, pp. 1214–1221.
https://doi.org/10.2514/1.25914

[33] Eça, L., and Hoekstra, M., "A Procedure for the Estimation of the Numerical Uncertainty of CFD Calculations Based on Grid Refinement Studies," *Journal of Computational Physics*, Vol. 262, April 2014, pp. 104–130.
https://doi.org/10.1016/j.jcp.2014.01.006

[34] Roache, P. J., "Quantification of Uncertainty in Computational Fluid Dynamics," *Annual Review of Fluid Mechanics*, Vol. 29, No. 1, 1997, pp. 123–160.
https://doi.org/10.1146/annurev.fluid.29.1.123

R. M. Cummings
Associate Editor